Underdamped Vortex Flow Devices

by

Amy E. Duwel

B.S. The Johns Hopkins University, Baltimore (1993)

Submitted to the Department of Electrical Engineering and Computer Science
in partial fulfillment of the requirements for the degree of

Master of Science in Computer Science and Engineering

at the

MASSACHUSETTS INSTITUTE OF TECHNOLOGY

May 1995

Author .....
Department of Electrical Engineering and Computer Science
March 28, 1995

Certified by .....
Terry P. Orlando
Professor of Electrical Engineering
Thesis Supervisor

Accepted by .....
Fredric R. Morgenthaler
Chairman, Departmental Committee on Graduate Students

Underdamped Vortex Flow Devices

by

Amy E. Duwel

Submitted to the Department of Electrical Engineering and Computer Science
on March 28, 1995, in partial fulfillment of the
requirements for the degree of
Master of Science in Computer Science and Engineering

Abstract

Discrete arrays of underdamped Josephson junctions can be used as oscillators and transistors for superconducting electronic applications. Both devices require that the system be biased in the flux-flow regime of its current-voltage characteristic. We present measurements and models for the performance of these devices. We find that the presence of a superconducting ground plane improves all of the device parameters except the transresistance. We further refined the devices by connecting two arrays in series. Magnetic coupling between adjacent loops of this array has a significant influence on the dynamics. A theoretical treatment shows that the coupling causes splitting of Fiske steps, zero-field steps, and flux-flow steps. Since we are considering device applications, our measurements focus on the splitting of the flux-flow step. This configuration produces steps at higher voltage levels with improved transresistances, but with degraded output resistance. The power and bandwidth are relatively unaffected. Inductively coupled arrays may be promising for some applications, but the dynamics must be more thoroughly investigated before this potential can be realized.

Thesis Supervisor: Terry P. Orlando
Title: Professor of Electrical Engineering

Acknowledgments

I would like to thank my advisor, Terry Orlando, for his guidance, patience, and faith in me. Thank you to Herre, for all of the time spent teaching me and answering questions, and for some quality coffee breaks. I am especially grateful to Enrique for his generous help and his friendship. I have also enjoyed working with Dave, Mauricio, and Shinya, and would like to thank them for all of their contributions. Thanks to Angela, Rich, and Charmaine, for their assistance, and for making our hallway the unique work environment that it is.

I would like to thank Danielle, Aman, and Cleo, my little family. Thank you to Jody, for our food-oriented friendship and for the witty jokes. Thank you to Roxanne, my collaborator and friend, and to Tasha, who is always there to remind me of what's important. Thanks to Carl, for following me to the library and all of the studying we didn't do. I'd like to thank my mother, who thinks I'm smart, and my brothers, who might not agree. I'd like to thank my big sister, who I still admire, and my little sisters, whom I adore. I'd like to thank my grandfather, who gets this instead of a budget. Thanks to my Uncle John, Danger Man, and to Uncle Hal, somewhere abroad. I'd like to thank Duncan Read, an astronomer, poet, and my mentor.

Finally, to Andreas and Alan: thank you for not allowing me to stop – your guidance and encouragement got me here. I will always look for opportunities to pass these gifts along.

I gratefully acknowlege both the Consortium for Superconducting Electronics and the National Science Foundation graduate fellowship program for their sponsorship.

Contents

List of Figures

List of Tables

Chapter 1

Introduction

The Josephson junction is the fundamental element of superconducting electronics, playing much the same role as the transistor in semiconductor electronics. A thorough understanding of the Josephson junction's characteristics and performance is crucial to the development of superconducting electronics. Already, SQUIDs (superconducting quantum interference devices) have made an impact on medical technology, and single Josephson junctions are used as high-quality voltage standards. Long Josephson junctions (junctions with lengths larger than the magnetic field penetration depth, λ_J) have been studied extensively, and can perform as both transistors and oscillators. However, devices made from long junctions have clear limitations, which can be overcome by using parallel arrays of short junctions instead.

To make our devices, we connect 54 short, underdamped junctions in parallel. A bias current is passed equally through each junction, and the DC voltage, equal to the average voltage across each junction, is measured across the row. This output voltage changes in the presence of a uniform DC magnetic field, applied by passing a current through a control wire aligned to the edge of the array.

Since two input currents result in an output voltage, the array can be thought of as the magnetic analog of the field-effect transistor (FET). In the field-effect transistor, a gate votage produces carriers (electrons or holes), and the drain-source bias voltage causes the

carriers to flow. The ratio of the resulting output current to the input gate voltage is called the transconductance. This is the key performance parameter of the FET. In long arrays of Josephson junctions, the control current produces a magnetic field which penetrates the array in discrete bundles called vortices. These can be thought of as "carriers". A bias current causes the vortices to move, resulting in an output voltage. Thus the device is called a vortex-flow transistor (VFT). The ratio of the output voltage to the input current is the transresistance. This is the parameter we wish to optimize for the VFT.

Overdamped junctions function well as transistors. Overdamped long junctions have shown transresistances of about $0.2\,\Omega$ [1, 2], while discrete arrays have been fabricated with transresistances of $0.43\,\Omega$ [3]. Underdamped junctions operate quite differently, but may also offer promising device characteristics. Long underdamped junctions have exhibited transresistances of the order of $0.01\,\Omega$ [4]. Parallel arrays of underdamped junctions compete with these devices, operating with transresistances of about $1.8\,\Omega$ [6].

Because the DC output voltage of a Josephson junction or a Josephson junction array is proportional to the frequency of an AC current in the system, they can be used as current-controlled oscillators. Underdamped arrays are well suited to this application, due to the particular dynamics of the system. Both long junctions and parallel arrays operate in the gigahertz regime with power levels of only nanowatts [5, 6]. The output impedence levels of such oscillators should be around 50Ω for optimal matching to other circuits. The reported impedence levels of long Josephson junctions are less than 1Ω, while parallel arrays offer an improved output impedence of about 10Ω [6].

The power levels of both continuous and discrete junction oscillators can be increased by placing several devices in series. Numerous studies done on stacked Josephson junctions [10, 13, 14] confirm this. It has also been shown that inductive and capacitive coupling between the junctions further complicates the dynamics of the stacked system, resulting in a unique IV characteristic. Although stacking of long Josephson junctions improves power levels, the coupling of a DC magnetic field into the system becomes increasingly difficult. In contrast, coupling magnetic fields into discrete arrays is straightforward, since they have a planar geometry. In addition, voltage probes can be easily placed along any row of a

discrete array, whereas the fabrication of stacked junctions with voltage probes along the middle layers is still a challenging problem.

In the following chapters, we will discuss some of the first measurements of discrete, inductively coupled arrays. We will compare these results with measurements of single arrays. We will present physical and mathematical models of the systems, which characterize important features of our data well.

Chapter 2

Background

2.1 Single Junction RSJ model

Superconducting devices based on the tunneling of superelectrons (Cooper pairs) are generally referred to as Josephson devices. An SIS (superconductor-insulator-supercondutor) Josephson junction is depicted in Fig. 2-1. In a superconducting material, all of the paired electrons behave coherently and can therefore be described by a single macroscopic wave-function, Ψ. The magnitude of this wave-function decays exponentially in the insulating region. However, if the insulator is thin enough, there will be some overlap of the wave-functions from the two superconductors. Associated with this overlap is a tunneling current, predicted by Brian Josephson in 1962. It can be shown [15] that, in the absence of any scalar or vector potentials, the supercurrent depends on the difference between the phases of the macroscopic wave functions in the two superconductors

$$\mathbf{J}_s = \mathbf{J}_c \sin(\theta_1 - \theta_2) \tag{2.1}$$

$\mathbf{J}_c$ is the critical current density of the junction, and it decays exponentially with the thickness of the insulator. In the presence of a magnetic field, the form of the above equation remains the same if we instead use the gauge-invariant phase difference

$$\mathbf{J}_s = \mathbf{J}_c \sin(\phi) \tag{2.2}$$

$$\phi = \theta_1 - \theta_2 - \frac{2\pi}{\Phi_o}\int_1^2 \mathbf{A}(\mathbf{r},t)\cdot d\mathbf{l} \tag{2.3}$$

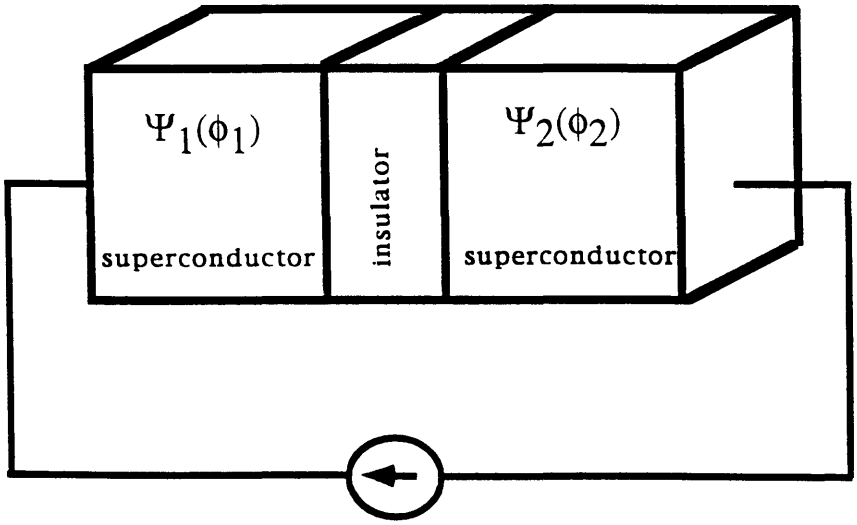

Figure 2-1: Josephson tunnel junction.

With the approximation that the current and phase are uniform over the cross-section of the junction, we can derive the lumped-element current-phase relation [15]

$$i = I_c \sin\phi(t) \tag{2.4}$$

It can also be shown that a time-dependent phase difference results in a voltage across the junction [16]

$$\frac{d\phi}{dt} = \frac{2\pi}{\Phi_o}v \tag{2.5}$$

In equation 2.4, we see that the superconducting current does not exceed I_c. However, excess current can be passed through the junction via single, normal-electron tunneling. The geometry of the device also suggests that AC currents will be capacitavely conducted.

The SIS Josephson junction is often modeled as a simple parallel connection of these three current-conducting channels. This is referred to as the Resistively-Shunted-Junction (RSJ) model, and is presented in Fig. 2-2.

For a junction driven by a DC current source, Kirchoff's current law requires that

$$i = I_c \sin\phi + \frac{v}{R_n} + C\frac{dv}{dt} \tag{2.6}$$

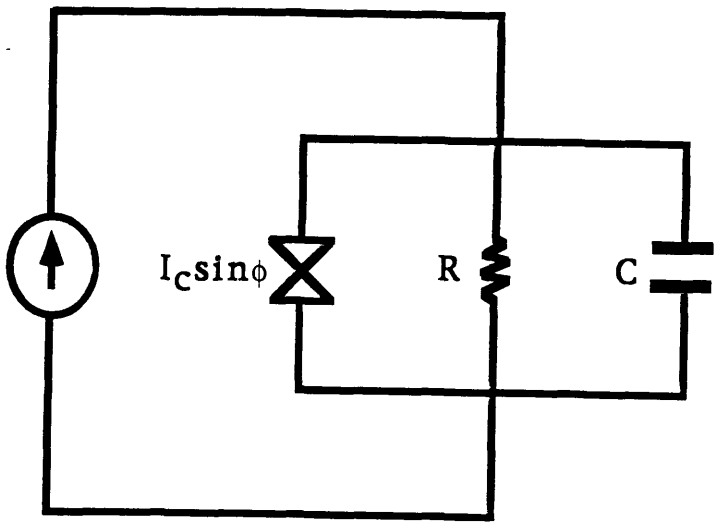

Figure 2-2: Resistively-Shunted Junction (RSJ) model of Josephson junction.

Writing the voltage in terms of phase differences, this becomes

$$i = I_c \sin\phi + \frac{\Phi_o}{2\pi R}\frac{d\phi}{dt} + C\frac{\Phi_o}{2\pi}\frac{d^2\phi}{dt^2} \tag{2.7}$$

For the resistance, R, we usually use the normal-state resistance, R_n, of the junction. When the junction voltage is below the superconducting gap voltage, $2\Delta/e$ (sometimes called the sub-gap region), the current and voltage do not have a simple linear relationship. An approximate resistance, R_{sg}, is sometimes used for R when the junction operates in the regime.

Even this simple model of the Josephson junction results in a non-linear differential equation in ϕ which is difficult to solve. However, it has been noted that this system is described by the same equations as the damped, driven pendulum. In hopes of gaining some physical insight, the two systems are often compared. Pursuing this analogy, we re-write the dynamical equation:

$$\ddot{\phi} + \frac{1}{R_n C}\dot{\phi} + \frac{1}{CL_J}\sin\phi = \frac{i}{I_c C L_J} \tag{2.8}$$

$$\text{where} \quad L_J = \frac{\Phi_o}{2\pi I_c}$$

For small phase differences, such that $\sin\phi \approx \phi$, the equation can be satisfied by solutions

of the form $\phi = e^{st}$ for s such that

$$s = \frac{-1}{2RC} \pm \left[\left(\frac{1}{2RC} \right)^2 - \frac{1}{CL_J} \right]^{1/2} \equiv -\alpha \pm \sqrt{\delta} \tag{2.9}$$

Then the homogeneous solution for $\phi(t)$ is:

$$\phi(t) = e^{-\alpha t}[A_1 e^{\sqrt{\delta}t} + A_2 e^{-\sqrt{\delta}t}] \tag{2.10}$$

The homogeneous solution will be a decaying, oscillating function for $\delta < 1$ (that is, for $R^2C/L_J > 1/4$), and will be a smoothly decaying exponential for $\delta > 1$. Therefore, the quantity $R^2C/L_J \equiv \beta_c$ is used to identify the degree of damping in the system, and is called the Stewart-McCumber parameter [17, 18]. In mechanics, the degree of damping in an oscillating system is customarily described in terms of a quality factor, Q. This is related to the Stewart-McCumber parameter by $Q^2 = \beta_c/2$.

2.2 Sine-Gordon Equation for Parallel Arrays

Parallel arrays of Josephson junctions, as depicted in Fig. 2-3, are sensitive to applied magnetic fields. Consider, first, the case of a continuous perfectly conducting loop. In response to an applied flux, this system generates a mesh current, I^m, to expel the flux. The inductance of the loop, L, characterizes this response: $LI^m = -\Phi_{\text{app}}$. This is also true of a superconducting loop if it is initially cooled to its superconducting state in zero field. In contrast, a superconducting loop which is broken by one or more tunnel barriers allows the field to penetrate the loop through the tunnel barriers. Even when cooled to the superconducting state in no initial field, this system is described by: $LI^m = \Phi^m - \Phi_{\text{app}}$, where Φ^m is the flux threading the loop. If the mutual inductance between all pairs of loops in an N-junction array is included, the equation becomes

$$\sum_{i=1}^{N-1} L_{i,j} I_i^m = \Phi_j^m - \Phi_{\text{app}} \tag{2.11}$$

where Φ_{app} is the applied flux per loop (cell) of the array and is assumed to be uniform.

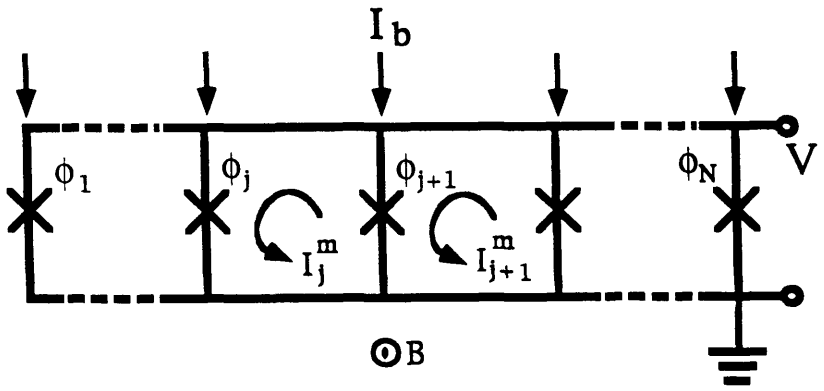

Figure 2-3: Parallel array of Josephson junctions. The phase difference across a junction is labeled ϕ_j. Circulating currents in each loop are marked I_j^m.

The flux through the loop is also related to the circulating currents through the phase of the macroscopic wave-function. The flux through one loop of the array determines the phase differences across the bordering junctions by

$$\frac{\Phi_j^m}{\Phi_o} = \frac{1}{2\pi}(\phi_{j+1} - \phi_j) + n_j \tag{2.12}$$

where n_j is an arbitrary integer, ϕ_j is the gauge-invariant phase difference across junction j, and the field is applied in the direction indicated in Fig. 2-3. This relationship is found using the supercurrent equation and the definition of the gauge-invariant phase difference [15]. The addition of the n_j arises from the fact that the phase of the macroscopic wave function can only be defined modulo 2π. Equations 2.11 can be combined with 2.12, giving

$$\frac{1}{\Phi_o}(\Phi_{\text{app}} + n_j\Phi_o) = \frac{1}{2\pi}(\phi_{j+1} - \phi_j) - \frac{1}{\Phi_o}\sum_{i=1}^{N-1} L_{i,j}I_i^m \tag{2.13}$$

Note that equation 2.13 is invariant under a change of the applied flux per unit cell by an integer number of flux quanta, since n_j is a free parameter. This is characteristic of all equations describing parallel arrays of Josephson junctions. In these discrete systems, it is therefore convenient to define a normalized field parameter, $f = \Phi_{\text{app}}/\Phi_o$, which is called the frustration.

Kirchoff's current laws indicate that the difference between the mesh currents is just the sum of the bias current and the junction current. Using the RSJ model and the Josephson relation, we find

$$I_j^m - I_{j-1}^m = I_b + I_c \sin\phi_j + \frac{\Phi_o}{2\pi R_n}\frac{d\phi_j}{dt} + \frac{\Phi_o C}{2\pi}\frac{d^2\phi_j}{dt^2} \tag{2.14}$$

where R_n has been used for the junction resistance, and I_b is the bias current. This can be combined with equation 2.13 to give an equation in ϕ only. For the simple case where only self-inductances are included ($\sum_i L_{i,j} I_i^m = L_{jj} I_j^m = L_s I_j^m$), this gives the discrete sine-Gordon equation

$$\Lambda_J^2[\phi_{j+1} + \phi_{j-1} - 2\phi_j] - 2\pi\Lambda_J^2(n_j - n_{j-1}) - \beta_c\ddot{\phi}_j - \dot{\phi}_j = \sin\phi_j + \frac{I_b}{I_c} \tag{2.15}$$

The time has been normalized to $\tau_J = 1/\omega_J \equiv \Phi_o/2\pi I_c R_n$. We have also used $\Lambda_J^2 = \Phi_o/2\pi I_c L_s = L_J/L_s$ and $\beta = R_n^2 C/L_J$. The current-voltage characteristic for a current-biased, N-junction array can be found by solving the above equation, with the following boundary conditions

$$\Lambda_J^2[\phi_2 - \phi_1 + 2\pi(n_1 + f)] - \beta_c\ddot{\phi}_1 - \dot{\phi}_1 = \sin\phi_1 + \frac{I_b}{I_c} \tag{2.16}$$

$$\Lambda_J^2[\phi_{N-1} - \phi_N - 2\pi(n_{N-1} + f)] - \beta_c\ddot{\phi}_1 - \dot{\phi}_1 = \sin\phi_1 + \frac{I_b}{I_c} \tag{2.17}$$

To solve this system of equations, especially if all inductances are included, it is helpful to write the equations in matrix form. We define $\mathbf{L}$ as the inductance matrix, normalized to L_s, $\mathbf{M}$ as a loop-sum operator (with built-in boundary conditions), and ϕ as the phase vector. The equations can now be written as

$$\Lambda_J^2\mathbf{M}^T\mathbf{L}^{-1}[2\pi(n - f) - \mathbf{M}\phi] = \frac{I_b}{I_c} + \sin\phi + \beta_c\ddot{\phi} + \dot{\phi}. \tag{2.18}$$

Thus we have an ordinary differential equation describing the evolution of the phases across an N-junction array. Since n is an arbitrary integer, this system is invariant under integral changes in f.

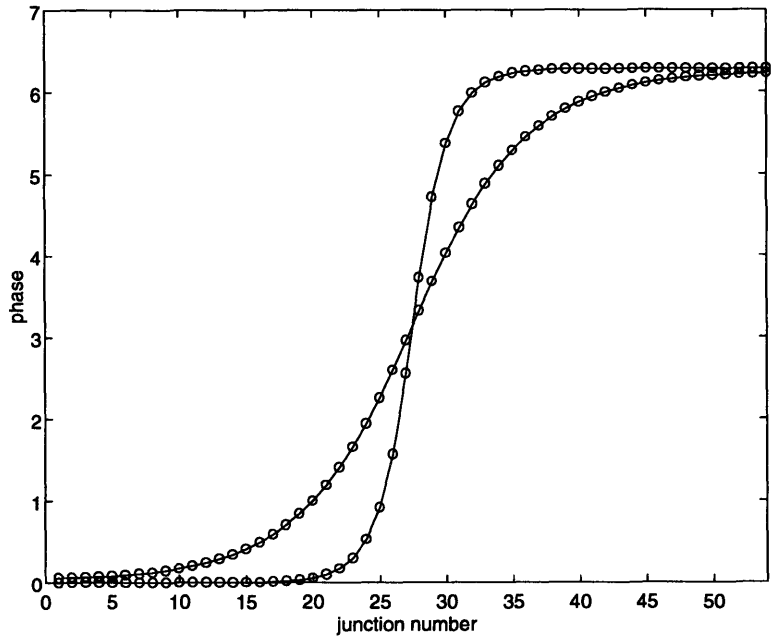

Figure 2-4: Phase distribution across a parallel array of 54 junctions. A vortex is in the center of the array. Points mark the value of the phase at each junction, and the solid line represents the arctan approximation. The steeper curve is the result for $\Lambda_J^2 = 3$, while the second was calculated using $\Lambda_J^2 = 30$.

2.3 Numerical Analysis

2.3.1 Static Behavior

To fully characterize the 1D array, it is helpful to examine its static properties in the presence of a magnetic field. In this case, the time-derivatives of the phases vanish, and the system of equations becomes

$$\Lambda_J^2 \mathbf{M}^T \mathbf{L}^{-1} [2\pi(n - f) - \mathbf{M}\phi] = \frac{I_b}{I_c} + \sin\phi. \tag{2.19}$$

A solution can be found by using a quasi-Newton-Raphson method. We find that this system supports a special type of solution, called a vortex. In a one-dimensional array, a vortex is characterized by the phase distribution shown in Fig. 2-4. A long Josephson

junction supports a similar distribution. In the long junction case, however, an analytic expression for this phase solution is possible [19]. The discrete version of the expression, is given by

$$\phi_j = 4 \arctan \left[\exp \left(\frac{j - j_o}{\Lambda_J} \right) \right] \tag{2.20}$$

where j_o is the center of the vortex. The solid line in Fig. 2-4 shows that this agrees well with simulations. We also see that the final phase configuration depends on the value of Λ_J. As Λ_J is increased, the vortex becomes more spread out across the array. Thus Λ_J is referred to as the penetration depth. For very large Λ_J (small L_s), an entire vortex does not fit into the array.

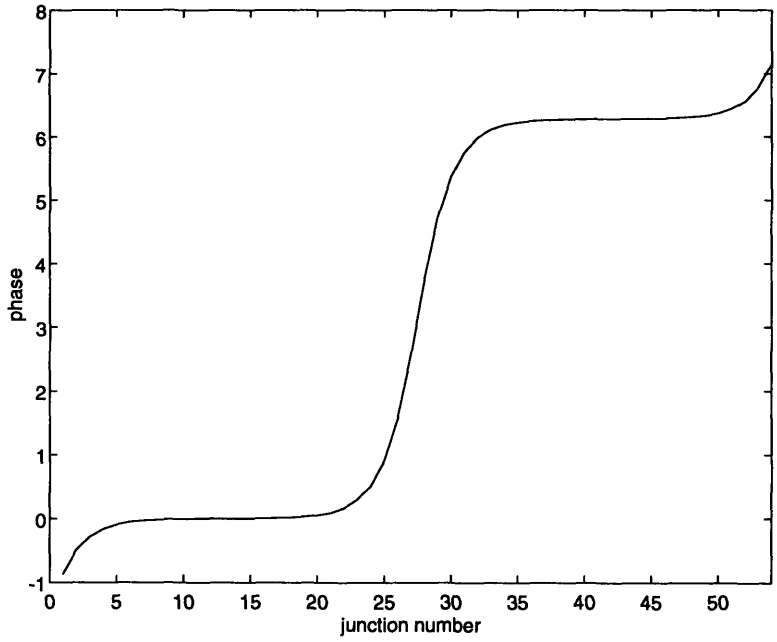

Figure 2-5: Phase distribution across an array of 54 junctions, for $f = 0.1$. The vortex is in the center of the array, and $\Lambda_J^2 = 3$.

When a magnetic field is applied, the phase distribution begins to change at the edges of the array (Fig. 2-5). Thus current, given by $I_j = I_c \sin \phi_j$, flows through the edge junctions. Magnetic flux also begins to penetrate the edges of the array, subject to the condition

$\Phi_j^m = \Phi_o(\phi_j - \phi_{j+1})/2\pi$. The current and flux profiles of a single vortex in a small external field appear in Fig. 2-6 and Fig. 2-7. The total amount of flux associated with the presence of a vortex can be found by calculating the area under the flux curve in Fig. 2-7. We find that, for values of Λ_J small enough to fit a vortex in the array, the total flux is always equal to Φ_o, or one flux quantum.

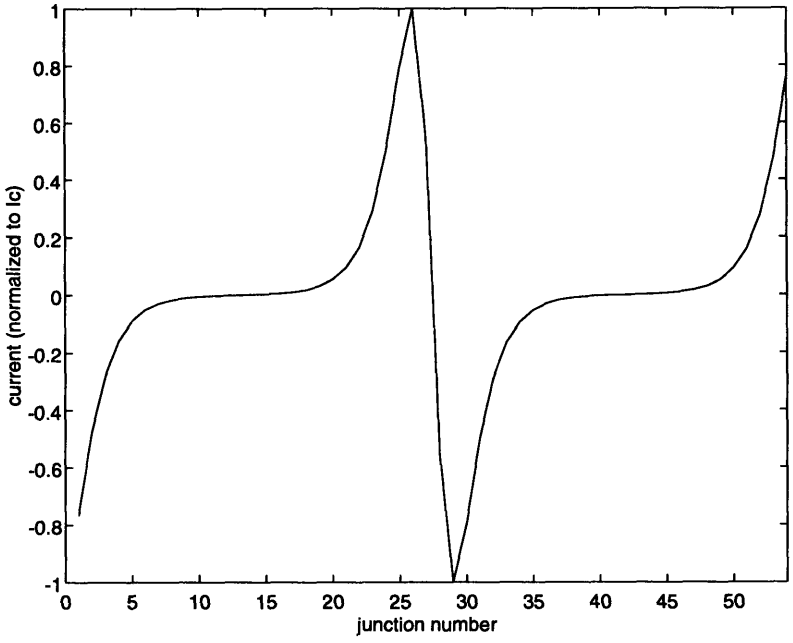

Figure 2-6: Current distribution across an array of 54 junctions, for $f = 0.1$. The vortex is in the center of the array, and $\Lambda_J^2 = 3$.

Associated with current and flux in an array are electric and magnetic energies. In the quasi-static limit, the energy stored in our system can be written in terms of the terminal variables, voltage and current

$$W = \int iv\,dt \tag{2.21}$$

In this limit, we can use a lumped-element circuit model of the system to estimate its internal energy. The electric energy stored in the superconducting channel of a single

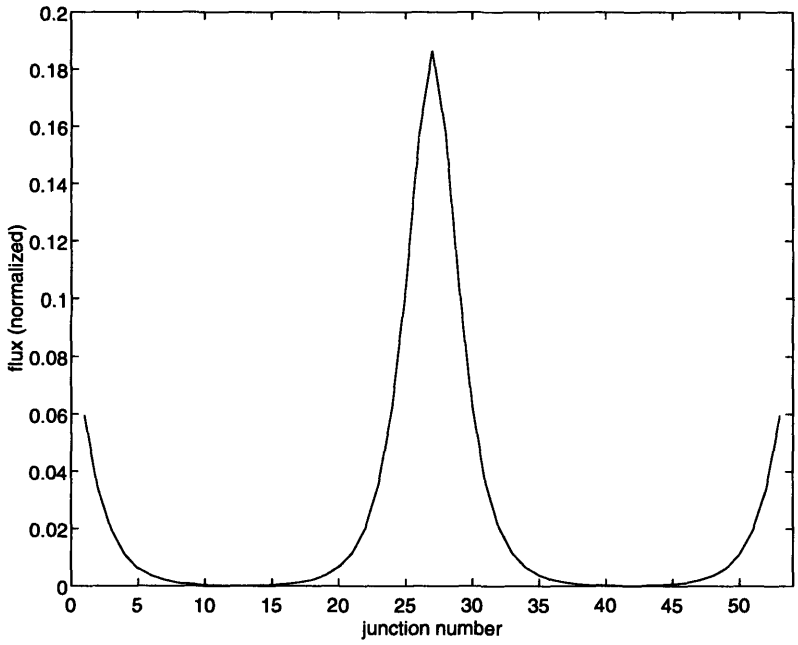

Figure 2-7: Flux distribution across an array of 54 junctions, for $f = 0.1$. The vortex is in the center of the array, and $\Lambda_J^2 = 3$.

Josephson junction is calculated by writing

$$i = I_c \sin\phi \tag{2.22}$$

$$v = \frac{\Phi_o}{2\pi}\frac{d\phi}{dt} \tag{2.23}$$

Substituting into the integral gives

$$W_e = \int_0^{t_o} (I_c \sin\overline{\phi}) \left(\frac{\Phi_o}{2\pi}\frac{\partial\overline{\phi}}{\partial t}\right) dt = \frac{\Phi_o I_c}{2\pi}(1 - \cos\phi) \tag{2.24}$$

The magnetic energy due to a circulating current, i^m, in a single loop of the array is calculated by writing the voltage as: $v = d\Phi/dt$. Then, for the simple case of self-inductance only,

$$W_m = \int i^m d\Phi = \int i^m L_s \, di^m = \frac{1}{2} L_s (I^m)^2 \tag{2.25}$$

The sum of W_e and W_m over the array gives the internal energy of the system. We can use this calculation to determine the value of the applied magnetic field at which it becomes

energetically favorable for a vortex to exist in the system (see Appendix A). This is called the thermodynamic critical field, H_{c1}. In a continuous long Josephson junction, this field was estimated to be $H_{c1} = 2\Phi_o/(\pi^2\lambda_J h\mu_o)$, where h is the thickness of the tunnel barrier [20, 15]. The long Josephson junction can be modeled as a discrete array (see Appendix B), and the critical field translates into $H_{c1} = 2\Phi_o/(\mu_o\pi^2\Lambda_J p^2)$. In terms of the frustration, the long Josephson junction model gives $f_{c1} = 2/(\pi^2\Lambda_J)$. Fig. 2-8 compares this estimate to the static calculation of $f_{c1}(\Lambda_J)$. For this calculation, the long Josephson junction model works well.

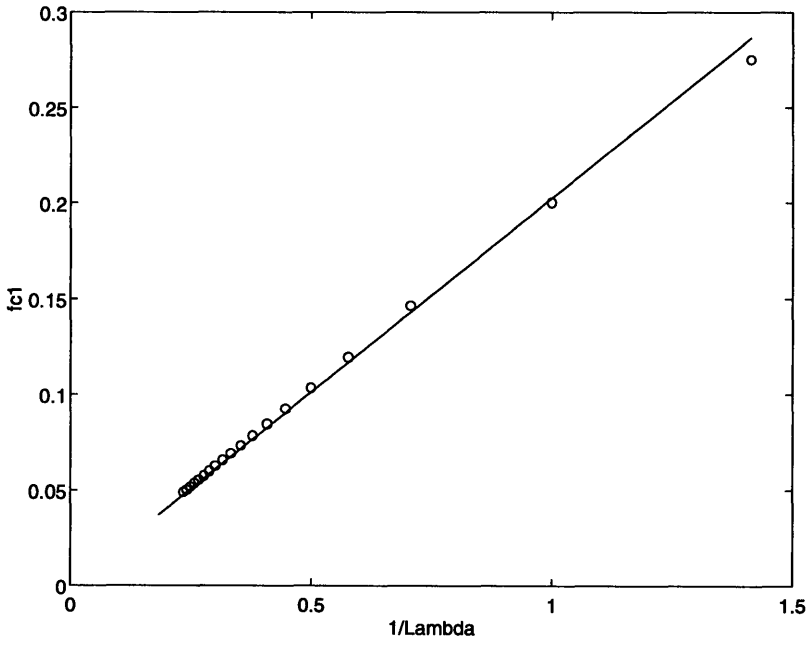

Figure 2-8: Critical field for a discrete array of 54 junctions. The points mark the result of static simulations. The solid line represents an approximation obtained from the long junction model.

2.3.2 Dynamic Behavior

A solution to the full dynamic equation 2.18 can be found numerically. The continuous time derivatives are discretized, and the solution is advanced in small increments of time. Several methods have been devoloped to solve the problem. Our simulations [21] use the *fourth-order Runge-Kutta* scheme. Fig. 2-10 shows a simulated current-voltage curve of 54 junctions connected in parallel, and Fig. 2-9 shows the characteristic for 9 junctions in parallel. Steps appear in both iv's, where, for a particular voltage value, there is a steep rise in current. These structures are also present in our experimental data.

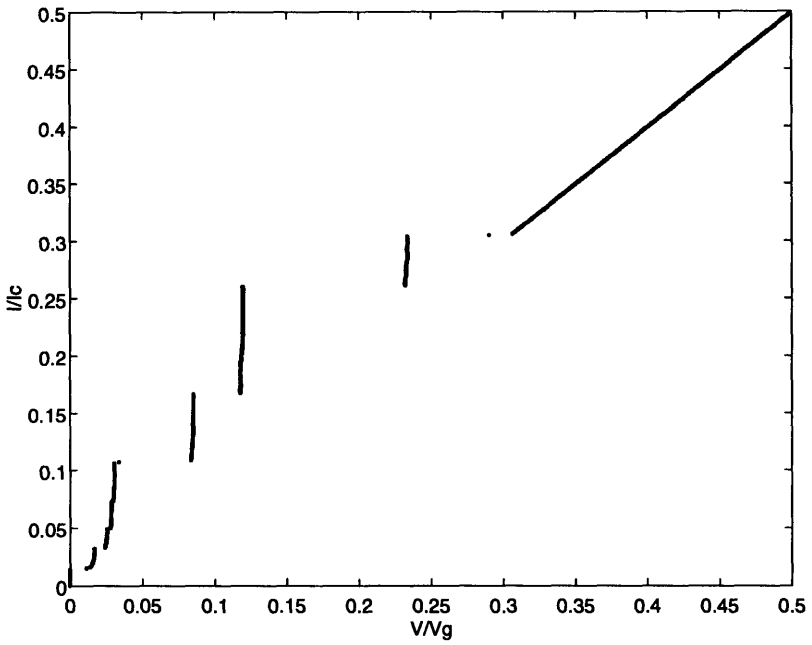

Figure 2-9: Simulated current-voltage characteristic for an array of nine junctions. The parameters used were $\beta = 445$ and $\Lambda_J^2 = 2.87$.

Using the Josephson relation, we can write the voltage position of a resonance in terms of the average frequency of the juncion phases ($\omega = \dot{\phi}$). These resonant frequencies can then be calculated using a linear instability analysis of the junction phases [22]. A similar approach has also been used in long Josephson junctions to predict Fiske modes [23], zero-field steps

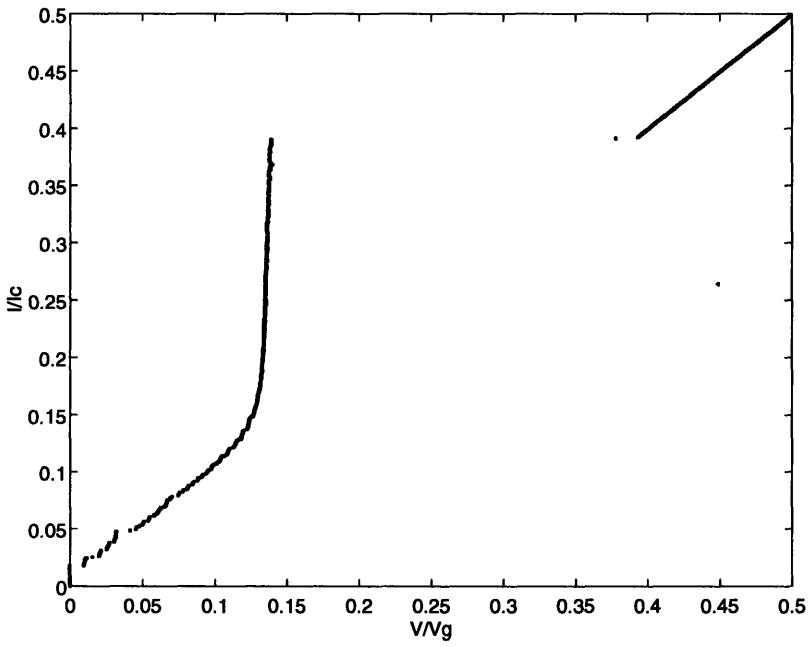

Figure 2-10: Simulated current-voltage characteristic for an array of 54 junctions. The parameters used were $\beta = 445$ and $\Lambda_J^2 = 2.87$.

[24], and the Eck step [25].

To find the resonances of this system, consider the simple case of large junction resistance (no damping) and include only self-inductances. Without normalizing time, equation 2.15 becomes

$$\Lambda_J^2[\phi_{j+1} + \phi_{j-1} - 2\phi_j] - CL_J\ddot{\phi}_j = \sin\phi_j + \frac{I_b}{I_c} \tag{2.26}$$

The boundary conditions are

$$\Lambda_J^2[\phi_2 - \phi_1 + 2\pi(n_1 + f)] - CL_J\ddot{\phi}_1 = \sin\phi_1 + \frac{I_b}{I_c} \tag{2.27}$$

$$\Lambda_J^2[\phi_{N-1} - \phi_N - 2\pi(n_{N-1} + f)] - CL_J\ddot{\phi}_N = \sin\phi_N + \frac{I_b}{I_c} \tag{2.28}$$

We can also satisfy the boundary conditions by defining the phases of artificial junctions at the ends of the array such that

$$\phi_0 = \phi_1 + 2\pi f \tag{2.29}$$

$$\phi_{N+1} = \phi_N - 2\pi f \tag{2.30}$$

Then equation 2.26 holds for all N junctions, and the boundary conditions are given above.

We approximate that the phase can be written as the sum of a known linear function (in time and space) and a very small unknown function in time and space.

$$\phi_j = \phi_j^{(0)} + u_j \tag{2.31}$$

The known functions, $\phi^{(0)}$, must satisfy both the dynamical equation, 2.26, and the boundary conditions, 2.30. We require that $\phi_j^{(0)} \gg u_j$ so that $\sin\phi_j \approx \sin\phi_j^{(0)} + u_j \cos\phi_j^{(0)}$. When this is substituted into equation 2.26, the result is an equation in u_j,

$$\ddot{u_j} + \frac{1}{CL_J}\cos\phi_j^{(0)} u_j - \frac{1}{L_s C}[u_{j+1} + u_{j-1} - 2u_j] = 0 \tag{2.32}$$

Since $\phi_j^{(0)}$ alone must satisfy the boundary conditions, u_j must satisfy

$$u_0 = u_1 \tag{2.33}$$

$$u_N = u_{N+1} \tag{2.34}$$

We will look for periodic solutions of these small perturbations in phase. When the periodic solutions become unstable, we expect a resonance to occur. Although u_j is a finite function, we can treat it mathematically as an infinite, periodic function, as long as we use the correct boundary conditions (above). Thus we can write u_j as a Fourier series.

$$u_j = \sum_{m=0}^{N-1} A_m \cos\left[m\pi\frac{(j-1/2)}{N}\right] \tag{2.35}$$

The shifted cosine function satisfies the boundary conditions and the orthogonality condition

$$\sum_{j=1}^{N} \cos\left[\frac{m\pi(j-1/2)}{N}\right]\cos\left[\frac{n\pi(j-1/2)}{N}\right] = \frac{N}{2}\delta_{m,n} \tag{2.36}$$

Substituting the Fourier series into equation 2.32 and applying the orthogonality condition, we obtain

$$\sum_{m=0}^{N-1}[\ddot{A}_m\frac{N}{2}\delta_{m,n} + A_m\omega_m^2\frac{N}{2}\delta_{m,n}] = \tag{2.37}$$

$$-\frac{1}{CL_J}\sum_{m=0}^{N-1} A_m \sum_{j=1}^{N}\cos\left[\frac{n\pi(j-1/2)}{N}\right]\cos\phi_j^{(0)}\cos\left[\frac{m\pi(j-1/2)}{N}\right] = 0$$

where

$$\omega_m^2 = \frac{4}{L_s C} \sin^2\left(\frac{m\pi}{2N}\right) \tag{2.38}$$

If we include the coupling between adjacent loops of the array, the form of equation 2.38 remains unchanged. In this case, equation 2.38, becomes

$$\omega_m = \frac{2}{\sqrt{L_s C}} \left|\sin\left(\frac{m\pi}{2N}\right)\right| \left[1 + |M_h| \cos\left(\frac{m\pi}{N}\right)\right] \tag{2.39}$$

where M_h is the ratio of the coupling between adjacent loops and the self-inductance, and equation 2.39 is given to first order in M_h.

At this point it is clear that the solutions for u_j and its resonant frequencies depend on the choice of the solution $\phi_j^{(0)}$. For the special case of $f = 0$, the function $\phi_j^{(0)} = \omega t$ satisfies equation 2.26 and the boundary conditions. This choice also reduces equation 2.38 to a Mathieu equation.

$$\ddot{A}_n + A_n \left[\omega_n^2 + \frac{1}{CL_J} \cos\omega t\right] = 0 \tag{2.40}$$

The equation is linear, but is not easily solved because the coefficient of A_n is time-dependent. It is often referred to as a *parametric excitation*, since it acts as a periodic variation of the natural frequency, ω_n. Because the frequency ω is determined, $\cos\omega t$ can be treated as a driving term.

$$\ddot{A}_n + \omega_n^2 A_n = -A_n \frac{1}{CL_J} \cos\omega t \tag{2.41}$$

We can now look for resonances through an interation method. Consider the quantity $\epsilon = 1/(L_J C)$ to be a small parameter. We will proceed by solving equation 2.40 for $\epsilon = 0$ to obtain a first approximation to the solution, $A_n^{(0)}$. The difference between solution $A_n^{(0)}$ and A_n will be of order ϵ. $A_n^{(0)}$ will then be used on the right-hand side of equation 2.41 to obtain a more accurate estimate, $A_n^{(1)}$. For $\epsilon = 0$, we have

$$A_n^{(0)} = a \cos\omega_n t \tag{2.42}$$

Then the next order equation is

$$\ddot{A}_n^{(1)} + \omega_n^2 A_n^{(1)} = -\frac{a}{CL_J} \cos\omega t \cos\omega_n t \tag{2.43}$$

When the driving frequency on the right-hand side is equal to the free frequency on the left side, we expect the solution for $A_n^{(1)}$ to become unbounded and a resonance to occur. Writing $\cos\omega t \cos\omega_n t = \cos(\omega+\omega_n)t + \cos(\omega-\omega_n)t$, we can see that a resonance is possible at the frequencies: $\omega \pm \omega_n = \omega_n$, or $\omega = 2\omega_n$. Using the Josephson relation in equation 2.38, this means that steps are expected in the iv at the voltages

$$V_{ZFS} = \frac{2\Phi_o}{\pi\sqrt{L_s C}} \left|\sin\left(\frac{m\pi}{2N}\right)\right| \left[1 + |M_h| \cos\left(\frac{m\pi}{N}\right)\right] \tag{2.44}$$

These steps have, in fact, been observed, and are called zero-field steps (ZFS).

Obtaining possible resonance frequencies of u_j is straightforward in the $f = 0$ case, since the solution $\phi_j^{(0)}$ has no spacial dependence. However, both the Fiske steps and the Eck step appear in the regime $f > 0$. In this case, calculation of the possible resonances becomes much more complex. The traditional calculation of Fiske resonances begins by writing the phase differences, ϕ_j, in equation 2.26 as the sum of a known solution, $\phi_j^{(0)}$ and a small perturbation, u_j. The solution $\phi_j^{(0)}$ is a traveling wave of the form $\phi_j^{(0)} = \omega t - kpj$, where $kp = 2\pi f$ and $\omega = 2\pi V/\Phi_o$. Then equation 2.26 becomes

$$\Lambda_J^2[u_{j+1} + u_{j-1} - 2u_j] - CL_J\ddot{u_j} = \sin(\phi_j^{(0)} + u_j) + \frac{I_b}{I_c} \tag{2.45}$$

In the past, this equation has been over-simplified by writing $\sin(\phi_j^{(0)} + u_j) \approx \sin\phi_j^{(0)}$. The resonances are then calculated by treating $\sin\phi_j^{(0)}$ as a driving term. However, the approximation is incorrect since the left side of equation 2.45 is first-order in u_j, while the right side is only zeroth order. Initial attempts to correctly derive the Fiske resonances and the Eck step are presented in reference [32]. In the parameter regime where the traveling wave solution for $\phi_j^{(0)}$ is appropriate, the authors find that resonances are possible at frequencies $\omega \approx \omega_m$, where ω_m is given by equation 2.38.

To verify that our measurements will be in this parameter regime, we can plot the phase solutions obtained from simulations and compare this to the postulated basic solution, $\phi_j^{(0)} = \omega t - kpj$. For $\Lambda_J^2 = 2.87$ and $\beta = 445$, the simulations are presented in Figures 2-11, 2-12, and 2-13. In the time domain, it is clear that the phase can be treated as the sum of a linear function and a small perturbation. As expected, the slope of the linearization matches

the average voltage. The spacial distribution is more complicated, although the slope of the linear fit does match the expected wavelength of the basic solution, $\phi^{(0)}$. It is possible, then, that this solution will suffice to predict resonances. However, in this pararmeter regime, the theory should be compared carefully with measurements and simulations. We expect resonances at $\omega \approx \omega_m$, and the Fiske steps to appear at voltages

$$V_{FS} = \frac{\Phi_o}{\pi\sqrt{L_s C}} \left|\sin\left(\frac{m\pi}{2N}\right)\right| \left[1 + |M_h| \cos\left(\frac{m\pi}{N}\right)\right] \tag{2.46}$$

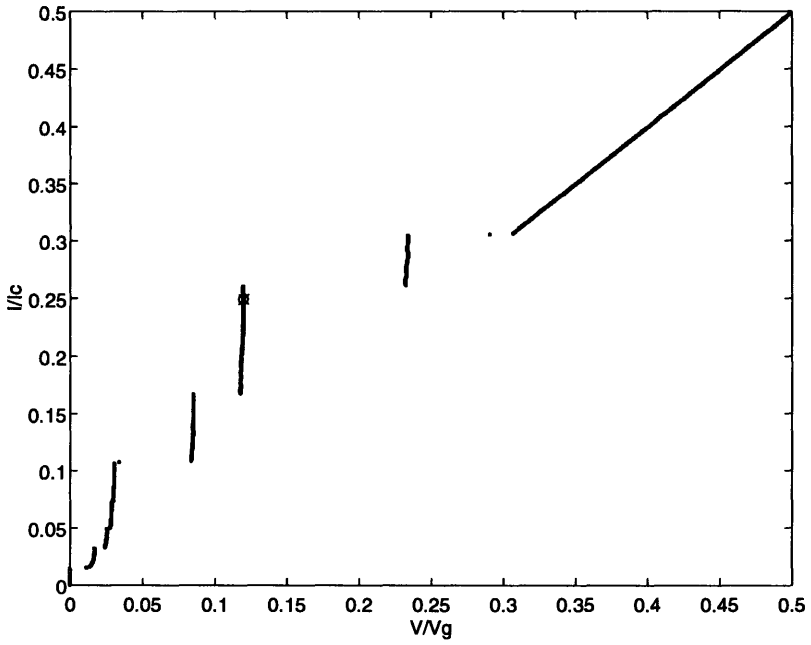

Figure 2-11: Simulated current-voltage characteristic for an array of 9 junctions. The parameters used were $\beta = 445$ and $\Lambda_J^2 = 2.87$. A point is marked on one of the steps where the phase solutions will be followed in time.

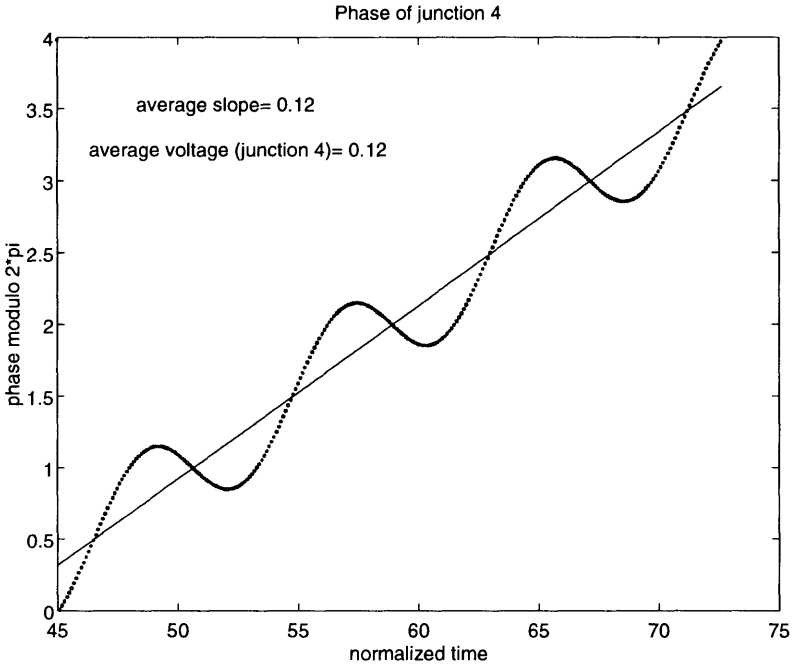

Figure 2-12: The phase evolution of a single junction.

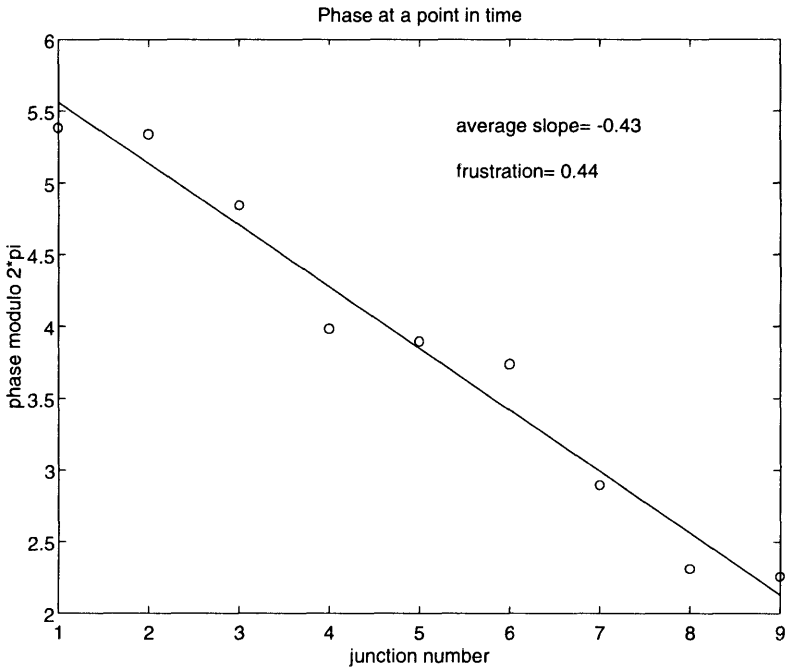

Figure 2-13: Distribution of the phases across the entire array, at a single point in time.

In an array where the number of junctions is large, a single Eck step appears, as in Fig. 2-10. A mathematical analysis for this resonance has not yet been formulated, although physical arguments suggest that the dispersion relation is the same as for Fiske steps. The application of a magnetic field to the system causes a vortex array to penetrate, with periodicity f. A bias current causes the vortex array to move, and the changing flux at the end of the array is measured as a DC voltage. Since the system is very long and has finite damping, we do not expect reflections at one end of the array to reach the other. Thus, both $\phi_j^{(0)}$ and u_j will have traveling wave solutions, with the same wavelength, $kp = 2\pi f$. If u_j is now written as a sum of traveling waves, an equation similar to 2.38 will be obtained, with the characteristic frequency

$$\omega^2 = \frac{4}{L_s C} \sin^2(\pi f) \tag{2.47}$$

This translates into a voltage

$$V_E = \frac{\Phi_o}{\pi\sqrt{L_s C}} |\sin(\pi f)| [1 + |M_h| \cos(2\pi f)] \tag{2.48}$$

This is also referred to as a flux-flow step, since it originates from a moving vortex array, traveling with maximum phase velocity, $\omega(k)$.

Using a linear analysis, we calculated resonant frequencies of the system which, as shown in reference [26], closely match experimental results. It turns out that Fiske steps appear at frequencies which can be predicted by completely neglecting the non-linear term of equation 2.26. Physically, this amounts to modeling the Josephson junction array as a simple linear system which has the same natural frequencies. The circuit model, depicted in Fig. 2-14, is that of a lossless TEM transmission line. Comparing this with the RSJ model of a single junction, we see that both the resistive channel and the Josephson channel are neglected. The capacitive impedence of the junction must be much smaller than the impedences associated with R and L_J. Using the transmission line circuit, we can write an equation relating the voltages at adjacent nodes, which is similar in form to the phase equation 2.26. For self-inductances only, we have:

$$V_{n+1} + V_{n-1} - 2V_n - L_s C \ddot{V}_n = 0 \tag{2.49}$$

The transmission line analysis yields the same dispersion relation as that given above. Again, the resonant frequencies depend on wavelength. The boundary conditions are implemented by placing an infinite load at the output of the transmission line. It is then possible to find the poles of the imput impedence, Z_{in}. According to system theory, the pole of a network function (such as Z_{in}) is a natural frequency of the corresponding output network variable (V). We find that the poles of Z_{in} occur at $N\theta = m\pi$, where $\theta = k_m p$. This is the same condition found using the Fiske mode analysis.

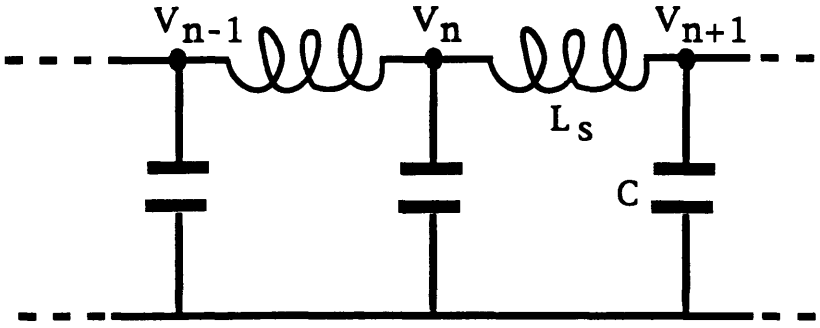

Figure 2-14: Lossless TEM transmission line: lumped element circuit model.

2.4 Inductively Coupled Arrays

In addition to one-dimensional arrays of junctions, we are also interested in the behavior of two such arrays connected in series. This circuit is depicted in Fig. 2-15. We can simulate the full dynamics (Fig. 2-16) and obtain an IV curve for the array in the presence of a magnetic field. Again, the distinguishing features are steps in the current-voltage curve. Comparing Fig. 2-16 to the one-dimensional array IV (for N=54), we see that there are now two steps, with two characteristic voltages. This splitting is also predicted by a linear instability analysis, as was done for the single array.

This system is governed by a similar set of equations. The gauge-invariant phase differ-

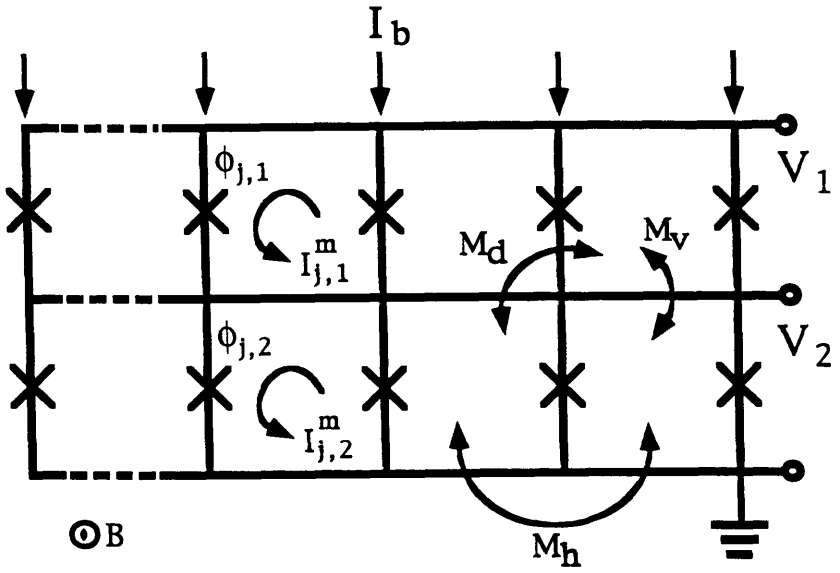

Figure 2-15: Circuit model of inductively coupled array. The junction phases are designated $\phi_{j,1}$ in the top row of the array, and in the bottom row they are $\phi_{j,2}$. The mutual inductance between two horizontally adjacent cells of the array is $M_h L_s$. Likewise, $M_v L_s$ and $M_d L_s$ are the inductances of vertically and diagonally adjacent cells, respectively.

ences across the junctions must satisfy

$$\phi_{j,1} - \phi_{j-1,1} = 2\pi \left(n_{j-1,1} + \frac{\Phi^m_{j-1,1}}{\Phi_o} \right) \tag{2.50}$$

$$\phi_{j+1,1} - \phi_{j,1} = 2\pi \left(n_{j,1} + \frac{\Phi^m_{j,1}}{\Phi_o} \right) \tag{2.51}$$

$$\phi_{j,2} - \phi_{j-1,2} = 2\pi \left(n_{j-1,2} + \frac{\Phi^m_{j-1,2}}{\Phi_o} \right) \tag{2.52}$$

$$\phi_{j+1,2} - \phi_{j,2} = 2\pi \left(n_{j,2} + \frac{\Phi^m_{j,2}}{\Phi_o} \right) \tag{2.53}$$

The total flux through each loop of the array, $\Phi^m_{j,1}$ and $\Phi^m_{j,2}$, must equal the sum of the applied flux and the induced flux. Including only nearest-neighbor inductances.

$$\Phi^m_{j,1} = \Phi_{\text{app}} + L_s I^m_{j,1} + M_h L_s (I^m_{j-1,1} + I^m_{j+1,1}) + M_v L_s I^m_{j,2} + M_d L_s (I^m_{j-1,2} + I^m_{j+1,2}) \tag{2.54}$$

A similar equation applies for $\Phi^m_{j,2}$. We have defined the inductive coupling between two horizontally adjacent loops to be $M_h L_s$. The coupling between vertically adjacent loops is $M_v L_s$, and the coupling between two diagonally opposite loops is $M_d L_s$. Kirchoff's current

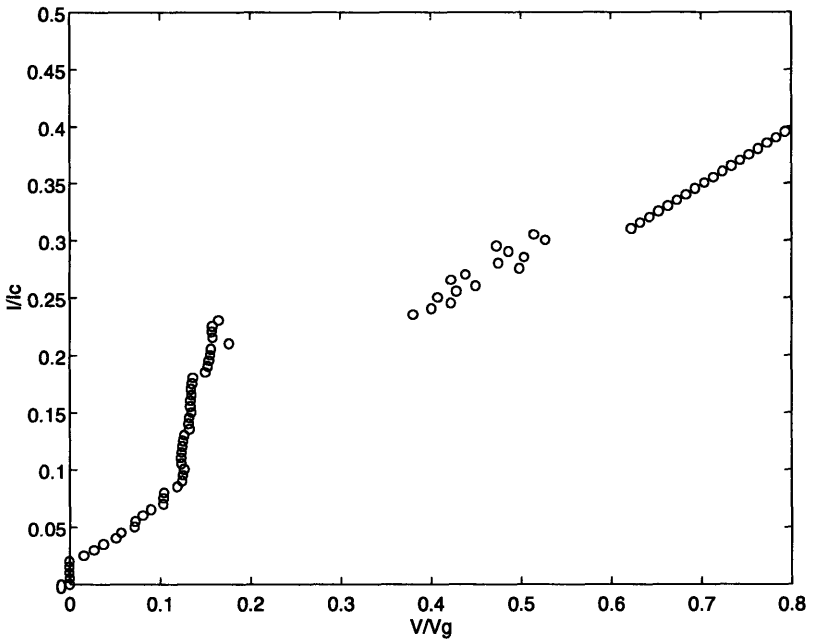

Figure 2-16: Simulated current-voltage characteristic for an inductively coupled array of 54x2 junctions. The parameters used were $\beta = 445$ and $\Lambda_J^2 = 2.87$.

laws can be used to relate the mesh currents to the junction currents. For the case of no bias current,

$$I_{j,1}^{RSJ} = I_{j,1}^m - I_{j-1,1}^m = I_c \sin\phi_{j,1} + C\frac{\Phi_o}{2\pi}\ddot{\phi}_{j,1} \tag{2.55}$$

Combining these governing equations, we can write an equation for each row in terms of the phases. To simplify the notation we define,

$$\phi_{j,1} \equiv \phi_j \tag{2.56}$$

$$\phi_{j,2} \equiv \psi_j \tag{2.57}$$

Then the equation for the first row becomes

$$\begin{aligned} \Lambda_J^2(\phi_{j+1} + \phi_{j-1} - 2\phi_j) - CL_J\ddot{\phi}_j - M_v CL_J\ddot{\psi}_j \qquad (2.58)\\ -M_h CL_J(\ddot{\phi}_{j+1} + \ddot{\phi}_{j-1}) - M_d CL_J(\ddot{\psi}_{j+1} + \ddot{\psi}_{j-1}) \\ = \sin\phi_j + M_h(\sin\phi_{j+1} + \sin\phi_{j-1}) + M_v \sin\psi_j + M_d(\sin\psi_{j+1} + \sin\psi_{j-1}) \end{aligned}$$

A similar equation holds for the second row. The boundary conditions are defined as in the last section,

$$\phi_0 = \phi_1 + 2\pi f \tag{2.59}$$

$$\psi_0 = \psi_1 + 2\pi f \tag{2.60}$$

$$\phi_{N+1} = \phi_N - 2\pi f \tag{2.61}$$

$$\psi_{N+1} = \psi_N - 2\pi f \tag{2.62}$$

Again, we write ϕ_j and ψ_j as sums of a known solution and small perturbations around that function.

$$\phi_j = \phi_j^{(0)} + u_j \tag{2.63}$$

$$\psi_j = \psi_j^{(0)} + v_j \tag{2.64}$$

Since both $\phi_j^{(0)}$ and $\psi_j^{(0)}$ must satisfy both the dynamical equation 2.59 and the boundary conditions 2.62, the equation for the small perturbations becomes

$$\Lambda_J^2(u_{j+1} + u_{j-1} - 2u_j) - CL_J\ddot{u_j} - M_vCL_J\ddot{v_j} = u_j \cos\phi_j^{(0)} + M_v v_j \cos\psi_j^{(0)} \tag{2.65}$$

$$\Lambda_J^2(v_{j+1} + V_{j-1} - 2v_j) - CL_J\ddot{v_j} - M_vCL_J\ddot{u_j} = v_j \cos\psi_j^{(0)} + M_v u_j \cos\phi_j^{(0)} \tag{2.66}$$

For the sake of simplicity, we temporarily neglect M_h and M_d. The effect of M_v is now clear. If we set $M_v = 0$, the equations become uncoupled, and replicate equation 2.32. The boundary conditioins are

$$u_0 = u_1 \tag{2.67}$$

$$v_0 = v_1 \tag{2.68}$$

$$u_{N+1} = u_N \tag{2.69}$$

$$v_{N+1} = v_N \tag{2.70}$$

Then we expand u_j and v_j as discrete Fourier series.

$$u_j = \sum_{m=0}^{N-1} A_m \cos\left[m\pi\frac{(j-1/2)}{N}\right] \tag{2.71}$$

$$v_j = \sum_{m=0}^{N-1} B_m \cos\left[m\pi\frac{(j-1/2)}{N}\right] \tag{2.72}$$

To investigate the ZFS, we let $f = 0$ and

$$\phi_j^{(0)} = \psi_j^{(0)} = \omega t \tag{2.73}$$

the equations become

$$A_n \left[\omega_n^2 + \frac{1}{CL_J}\cos\omega t\right] + \ddot{A}_n + M_v C L_J \ddot{B}_n + M_v B_n \cos\omega t = 0 \tag{2.74}$$

$$B_n \left[\omega_n^2 + \frac{1}{CL_J}\cos\omega t\right] + \ddot{B}_n + M_v C L_J \ddot{A}_n + M_v A_n \cos\omega t = 0 \tag{2.75}$$

where, as before,

$$\omega_n^2 = \frac{4}{L_s C}\sin^2\left(\frac{n\pi}{2N}\right) \tag{2.76}$$

The equations can be uncoupled by defining the normal coordinates

$$X_n = \frac{A_n + B_n}{2} \tag{2.77}$$

$$Y_n = \frac{A_n - B_n}{2} \tag{2.78}$$

Adding equations 2.75 and 2.75 gives and equation for x, while subtracting 2.75 from 2.75 yields and equation for y.

$$\ddot{X}_n + X_n\left(\frac{\omega_n^2}{1+M_v}\right) = -X_n\left(\frac{1}{CL_J}\right)\cos\omega t \tag{2.79}$$

$$\ddot{Y}_n + Y_n\left(\frac{\omega_n^2}{1-M_v}\right) = -Y_n\left(\frac{1}{CL_J}\right)\cos\omega t \tag{2.80}$$

We now have two uncoupled Mathieu equations. Note that the characteristic frequencies on the left side are not the same. Following the analysis of the previous section, define

$$X_n^{(0)} = x\cos\omega_n t = \frac{1}{2}(a+b)\cos\omega_n t \tag{2.81}$$

$$Y_n^{(0)} = y\cos\omega_n t = \frac{1}{2}(a-b)\cos\omega_n t \tag{2.82}$$

We obtain the resonance condition for the coordinate X_n

$$\omega = 2\omega_n\left(\frac{1}{1+M_v}\right)^{1/2} \tag{2.83}$$

The resonance condition for the Y_n coordinate is

$$\omega = 2\omega_n \left(\frac{1}{1 - M_v}\right)^{1/2} \tag{2.84}$$

Thus the system has two possible resonance frequencies. If we include all nearest-neighbor inductances, to first order, the resonances happen at

$$\omega_{\pm} = \frac{2}{\sqrt{L_s C}} \left|\sin\left(\frac{n\pi}{2N}\right)\right| \left[1 + (|M_h + M_d|)\cos\left(\frac{n\pi}{N}\right) \pm \frac{1}{2}|M_v|\right] \tag{2.85}$$

The frequency ω_+ corresponds to a resonance in the x-coordinate. Note that, for $A_n = B_n$, $y = 0$, and only ω_+ is possible. This is called the symmetric mode, since the small oscillations u_j and v_j are in phase. For $A_n = -B_n$, the small oscillations are out of phase, and the frequency ω_- is the that of the anti-symmetric mode.

This analysis predicts the frequencies of the ZFS in inductively coupled arrays and predicts that each zero-field step observed in the single array will now be split into two steps. As in the single array, Fiske resonances are expected at half the value of these frequencies, and the number of Fiske steps will double. Also, for large N, we see two Eck steps, corresponding to the two characteristic frequencies. The voltages of the Eck steps are now expected to be

$$V_{E\pm} = \frac{\Phi_o}{\pi\sqrt{L_s C}} |\sin(\pi f)|[1 + (|M_h + M_d|)\cos(2\pi f) \pm \frac{1}{2}|M_v|] \tag{2.86}$$

We will later compare this prediction to our experimental results.

Chapter 3

Experiments

3.1 Samples and Diagnostics

Arrays of underdamped Nb-NbO-Nb Josephson junctions were fabricated at HYPRES, Inc. [27]. This process offers junction current densities, J_c, of 100-1000 $\mathrm{A/cm^2}$. Junctions can be designed as small as $3\,\mu\mathrm{m} \times 3\,\mu\mathrm{m}$, and have a specific capacitance of $38\,f\mathrm{F/m^2}$. The junction characteristics and array inductances can be measured using a series of diagnostic procedures devoloped by van der Zant *et al.* [8]. This requires that a nine-junction parallel array be placed on every chip. The array has leads placed at one edge and at the center, as in Fig. 3-1.

The normal-state resistance of a single junction can be obtained by measuring the array resistance. Current is injected at the center, and voltage is measured across the leads at the edge. The array normal-state resistance is taken from the slope in the region after switching, and is ideally measured as close as possible to the critical temperature of niobium. The junction resistance is then approximately: $R_n = N R_{\mathrm{n,array}}$. The $I_c R_n$ product is a constant at a given temperature, and can be estimated from the Ambegaokar-Baratoff [28] relation: $I_c(T) = 0.86(\pi\Delta(T)/2eR_n)\tanh(\Delta(T)/2k_BT)$. At $T = 0$, $I_c R_n = 1.9\,\mathrm{mV}$. Thus, we can use R_n to confirm the value of the critical current density.

Measurements of the Fiske modes in an array provide values for M_h and for the product

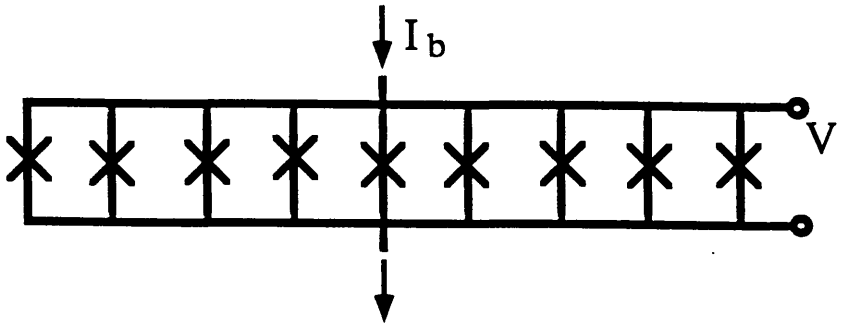

Figure 3-1: Parallel array of Josephson junctions, to be used for diagnostics.

L_sC. Fiske modes appear as steps in the current-voltage characteristics when a magnetic field is applied, and are most clearly observed when $\Lambda_J^2 > 2$. Fig. 3-2 shows measurements of a nine-junction array at T=4.2 K. As discussed in section 2.3.2, steps are expected at voltages of

$$V_m = V_o \sin\left(\frac{m\pi}{2N}\right)\left[1 + |M_h| \cos\left(\frac{m\pi}{N}\right)\right] \tag{3.1}$$

where $V_o = \Phi_o/(\pi\sqrt{L_sC})$ and $m = 1, 2, .., N-1$. The measured voltages of each Fiske mode are plotted against the above V_m expression to obtain values for V_o and M_h. Fig. 3-3 shows the data and fit.

The self-inductance, L_s, can be determined from a measurement of the array critical current, $I_{\text{c,array}}$, as a function of applied field. This method is based on static solutions for I_c in a long Josephson junction with current injected at one edge. Owen and Scalapino [29, 30] found that, near zero field, the relationship is linear and depends on the Josephson penetration depth, λ_J. In discrete arrays with current injected at the edge, a similar relation can be expected. In fact, when the long Josephson junction is modeled as a discrete array (see Appendix B), the slope calculated by Owen and Scalapino translates into: $\alpha = \Delta I_{\text{c.array}}/\Delta f = 4\pi\Lambda_J^2/N$, where we normalize $I_{\text{c,array}}$ to NI_c. Simulations have been used to find the exact relationship for discrete systems. When $N = 9$ and $\Lambda_J^2 < 9$, van der

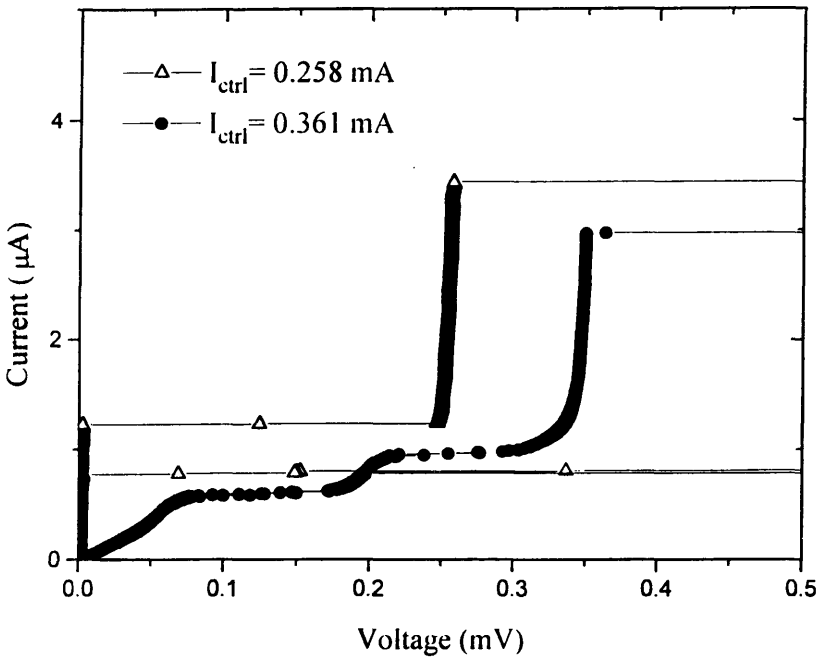

Figure 3-2: Measurement of N=9 array. The steps in the IV are called Fiske modes.

Zant *et al.* found that $\alpha = \Lambda_J^2/[1.43(1-2|M_h|)]$. Since M_h is found from the Fiske mode measurement, the slope of $I_c(f)$ near $f = 0$ determines Λ_J^2. Given the junction critical current, I_c, the value of Λ_J can be used to find L_s. In Fig. 3-4, we plot the measured critical current values of the same array, and estimate α. The Fiske mode analysis also determines the product of L_sC, so that the capacitance can be calculated.

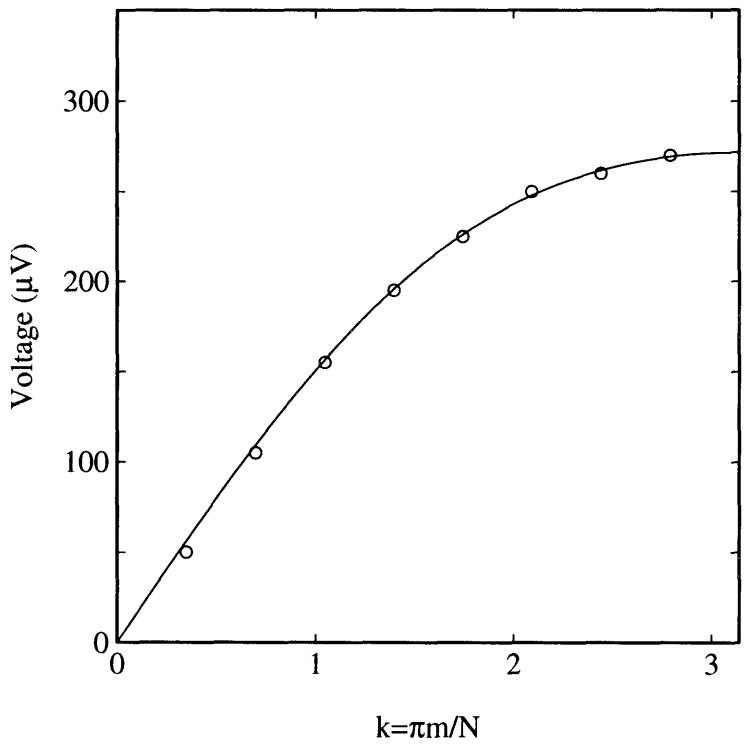

Figure 3-3: Voltage values of the Fiske steps versus mode number, m. The solid line is the fitted model.

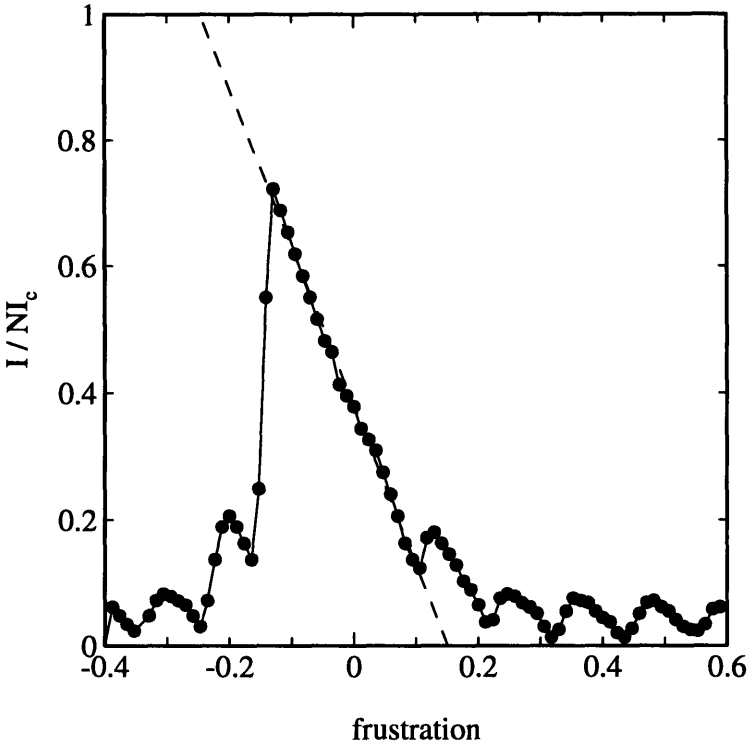

Figure 3-4: Critical current vs. frustration for a nine-junction array. Current is injected at the edge of the array. The dotted line represents a fit to the linear portion of the array, and has slope $\alpha = 2.512$.

The characteristics common to all of the devices measured are sumarized in table 3.1.

Sample Characteristics

Critical Current Density	$J_c = 89\,A/cm^2$
Junction Area	$A = 8\,\mu m^2$
Critical Current	$I_c = 6.3\,\mu A$
Normal-state Resistance	$R_n = 275\,\Omega$
Capacitance	$C = 300\,fF$
Loop Area	$A_l = 50\,\mu m^2$
Josephson Inductance	$L_J = 51\,pH$
McCumber Parameter	$\beta_c = 445$

Table 3.1: Sample Characteristics, T=4.2 K

Each of the devices on the chip can be subjected to a magnetic field through coupling to a superconducting control wire. The amount of magnetic flux supplied to the device, Φ_{app}, depends on the strength of the mutual inductive coupling, M_{ctrl}, and on the current in the control wire, I_{ctrl}. Writing the frustration in terms of the control current, this becomes:

$$f = \frac{M_{\text{ctrl}} I_{\text{ctrl}}}{\Phi_o} \tag{3.2}$$

3.2 Characteristics of Long Arrays

We have designed and measured arrays of 54 Josephson junctions, connected in parallel by superconducting Nb wires. A bias current, I_b, is applied uniformly to each junction through the use of resistors, and the voltage is measured with superconducting leads at the edge of the array. The control wire runs parallel to the edge of the array and is about 800 nm above it.

The magnetic field from I_{ctrl} injects vortices into the array. The bias current causes the vortices to move, thereby producing a voltage across the array, V, proportional to the

vortex velocity. For a fixed $I_{\rm ctrl}$, increasing I_b causes an increase in velocity, until the limiting electromagnetic phase velocity in the array is reached. At this point, increasing I_b further does not move the voltage beyond V_E, the Eck voltage. Thus there is a steep rise in the current, as shown in Fig. 3-5. For sufficiently high I_b, the voltage jumps to the gap voltage, V_g.

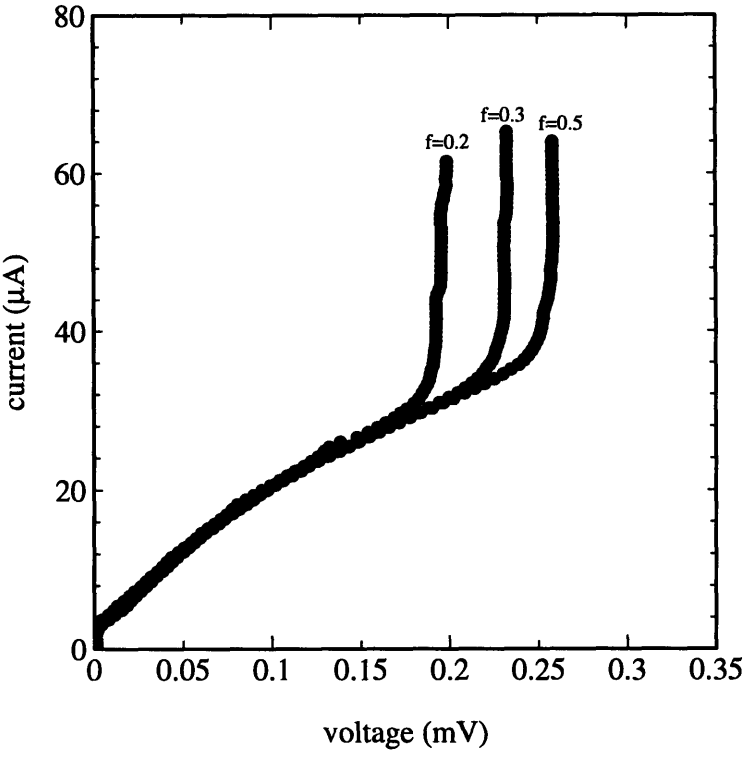

Figure 3-5: Measurements of an N=54 array. IV curves were taken for several different control currents (frustrations), at $T = 7\,K$.

When I_b is held constant and $I_{\rm ctrl}$ is increased (Fig. 3-6), V_E initially increases due to the higher density of injected vortices. However, as the data shows, V_E is periodic in $I_{\rm ctrl}$, with period $I_{\rm per}$. The lighter line in Fig. 3-6 shows the curve:

$$V_E = \frac{\Phi_o}{\pi\sqrt{L_s C}} \left| \sin\left(\frac{\pi M_{ctrl} I_{ctrl}}{\Phi_o} \right) \right| \tag{3.3}$$

This is taken from the linear analysis discussed in section 2.3.2, and equation 3.2 has been

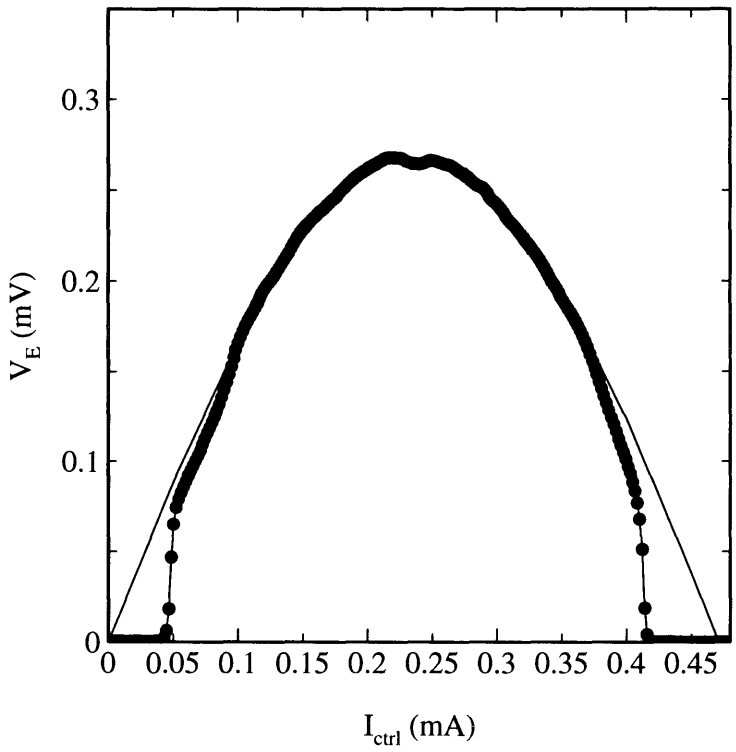

Figure 3-6: Measurements of an N=54 array. The array is biased at $I_b = 40\,\mathrm{mA}$, and the control current is swept between $I_{\mathrm{ctrl}} = 0 - 0.5\,\mathrm{mA}$. The lighter line represents the fitted model, with $V_{\mathrm{E,max}} = 0.27\,\mathrm{mV}$ and $I_{\mathrm{per}} = 0.47\,\mathrm{mA}$.

used for the frustration. We see that the period can be used to find $M_{\rm ctrl}$. At 4.2 K, our samples show a period of $I_{\rm per} = 0.45\,{\rm mA}$, implying $M_{\rm ctrl} = 4.6\,{\rm pH}$. We have used the diagnostic techniques described in section 3.1 to determine that $L_s = 16\,{\rm pH}$ and $C = 300\,{\rm fF}$. This gives a $V_{\rm E,max}$ of 0.3 mV, which corresponds well with the measured value of 0.27 mV.

Note that, for very small applied magnetic field, no Eck step appears at all. We can approximate the field value at which the Eck step appears by the thermodynamic critical field, discussed in section 2.3.1. Then the threshold, $f_{c1} = 2/\pi^2\Lambda_J$, will vary with temperature since Λ_J is temperature dependent.

3.3 1D Array Flux Flow Devices

From equations 3.3 and 3.2, we see that the array may be used as a current-controlled voltage source. The device is biased at I_b, with input current $I_{\rm ctrl}$ and output voltage V_E. When used in this manner, the device is often called a vortex-flow transistor (VFT). It is the magnetic analog of a field-effect transistor (FET), in which two control voltages produce an output current. In a FET, the transconductance is the key performance parameter. Likewise, in a VFT, the transresistance is the parameter we wish to optimize. The I-V characteristic is shown in Fig. 3-6.

The maximum output voltage is inversely proportional to $\sqrt{L_sC}$. The transresistance is defined as $r_m = V_{\rm out}/I_{\rm in}$. For our VFT, we approximate $r_m = \partial V_E/\partial I_{\rm ctrl}$, which increases as $M_{\rm ctrl}/\sqrt{L_sC}$ increases. Although the value of r_m depends on the operating point, we can obtain an upper limit by fitting the derivative of equation 3.3 to the derivative of our data. For the data shown in Fig. 3-6, we obtain a maximum transresistance of about 1.75Ω. The gain of our VFT can be defined as $G = I_{\rm out}/I_{\rm in}$. The output current depends on the load, and the gain is reduced to $G = r_m/R_L$, where R_L is the load resistance. Then, to obtain $G > 1$, we are limited to $R_L < r_m$. The output resistance, r_o, is given by the slope of $V(I_b)$ as the voltage approaches V_E. From Fig. 3-5, at f=0.5 $r_o = 0.31\,\Omega$. This parameter affects the operating range of the transistor and should be as small as possible.

The threshold current can be approximated from the critical field. Using equation 3.2,

we have

$$I_{th} = \frac{f_{c1}\Phi_o}{M_{\text{ctrl}}} \tag{3.4}$$

Using $f_{c1} = 2/(\pi^2\Lambda_J)$, I_{th} reduces to

$$I_{\text{th}} = \frac{4}{\pi}\Lambda_J\frac{L_s}{M_{\text{ctrl}}}I_c = 47.4\,\mu A \tag{3.5}$$

which closely matches the measured value of 50 μA.

This underdamped array may also be used as a current-controlled oscillator. The control current determines V_E, which, according to the Josephson relation, corresponds to a frequency, $\nu = V_E/\Phi_0$. For a given bias current, then, the frequency of the oscillator can be continuously tuned using I_{ctrl}. For our device, V_E ranges from 0 to 0.27 mV, giving a bandwidth of 130 GHz. As Figure 15 shows, the Eck step is quite steep. Thus there is a wide tolerence in the bias current value ($\approx 30\mu A$) which which is needed to produce a single output frequency. There is not yet an expression for either the linewidth of the output power or its AC amplitude. Based on the linewidth of a single junction oscillator, however, [6, 9], we expect the array linewidth to be proportional to r_o^2

$$\delta\nu = fN\frac{4\pi k_B T}{\Phi_o^2}\frac{r_o^2}{V_E/I_{\text{max}}} \tag{3.6}$$

The output impedence can be estimated by modeling the junction array as a transmission line, giving $Z_0 = \sqrt{L_s/C} \approx 10\,\Omega$. The maximum attainable power, $P = V_{\text{E,max}}I_{\text{E,max}}$, is about 8 nW.

Our simple models suggest that we can improve the output voltage and maximum power by decreasing L_s and C. We also expect higher voltages and possibly smaller linewidths from two arrays connected in series. In the following sections, we discuss configurations which address both of these issues.

3.4 Effects of Superconducting Ground Plane

In order to improve the device parameters, we placed the same arrays of Josephson junctions about 200 nm above a superconducting ground plane. We expected this configuration to increase the output power levels of the device by decreasing the value of L_s.

Our diagnostic measurements indicate that the effective self-inductance in the presence of a ground plane, L_s^{eff}, is lower than L_s by a factor of about 3.7 at 4.2 K. Measurements of I_{per} show that M_{ctrl} is also reduced by a factor of approximately 4.4 at 4.2 K. In addition, we have observed that, in the presence of a ground plane, the effective inductances increase with temperature. Fig. 3-7 shows L_s^{eff} and $M_{\text{ctrl}}^{\text{eff}}$ vs. temperature.

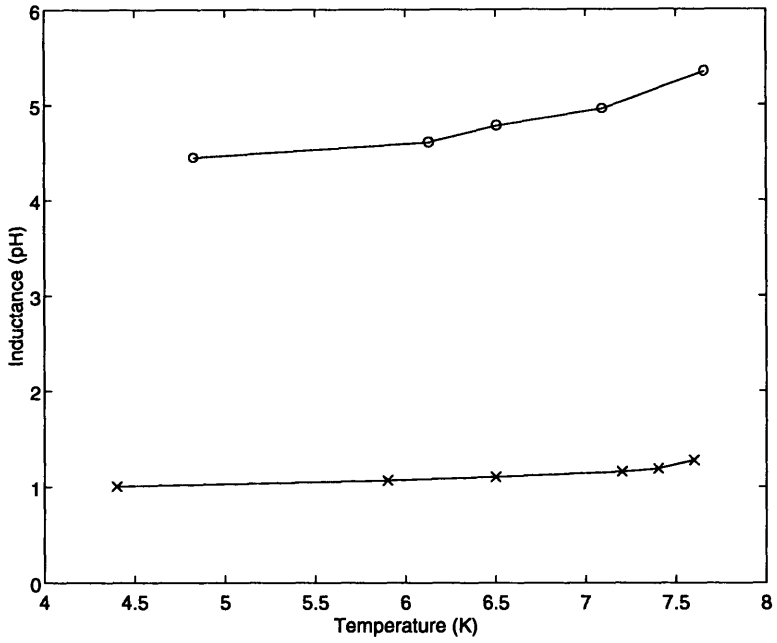

Figure 3-7: Self-Inductance measurements versus temperature. The data from the array above a ground plane is represented by circles, and the data for the array with no ground plane is marked with x's.

We can account for the temperature dependence of L_s using a very simple model. Instead of calculating the inductance of a thin superconducting loop above a thin ground plane, we estimate the inductance of two thin superconducting strips, with lengths equal to the inside perimeter of our loop. The superconducting loop of our circuit is so close to the ground plane that this transmission line model gives numbers which are quite close to our actual measurements. Fig. 3-8 shows the model and indicates how the dimensions are derived from

our mask designs. For penetration depths, λ, comparable to the strip thickness, b, the DC self-inductance of the transmission line is [15]

$$L_s = \frac{\mu_o l}{w}\left(h + \frac{2\lambda^2}{b}\right) \tag{3.7}$$

where

$$\lambda(T) = \frac{\lambda_o}{\sqrt{1-(T/T_c)^4}} \tag{3.8}$$

In niobium, $\lambda_o = 85$nm and $T_c = 9.25$ K. To test our model, we plot the measured inductance versus $(\lambda(T)/\lambda_o)^2$. We fit the model to the data by varying the slope and the intercept of the line given by equation 3.7. The result, shown in Fig. 3-9, gives values of $h = 505\,nm$ and $\lambda_o = 89.5\,nm$. In Fig. 3-10, we plot both the data and the model inductances versus temperature, showing that the model works well.

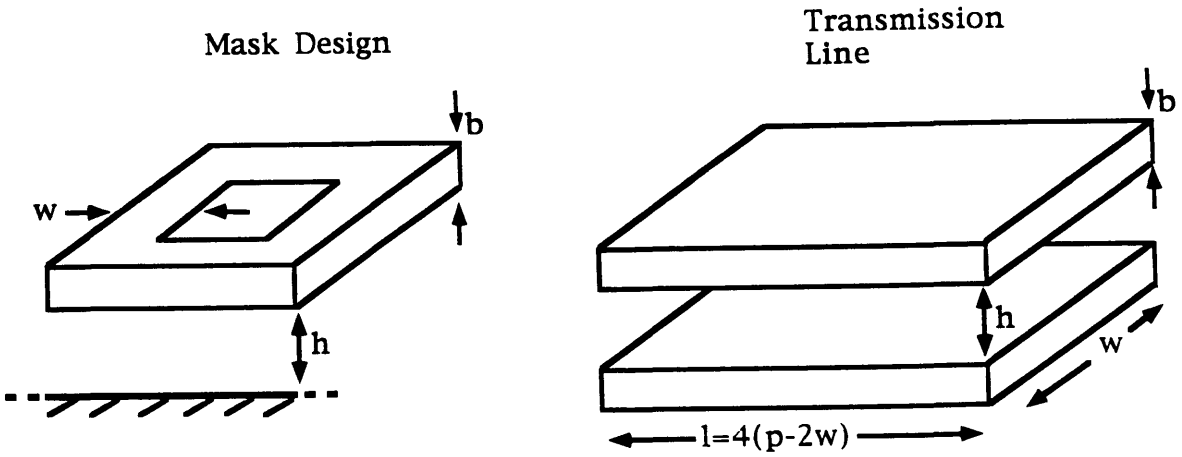

Figure 3-8: Transmission line model for calculating the self-inductance of a single loop of the array. In our mask designs, we have the following dimensions: $b = 0.1\,\mu$m, $w = 3\,\mu$m, $p = 10\,\mu$m. Although the structure is not completely planar, we approximate that $h \approx 0.5\,\mu$m.

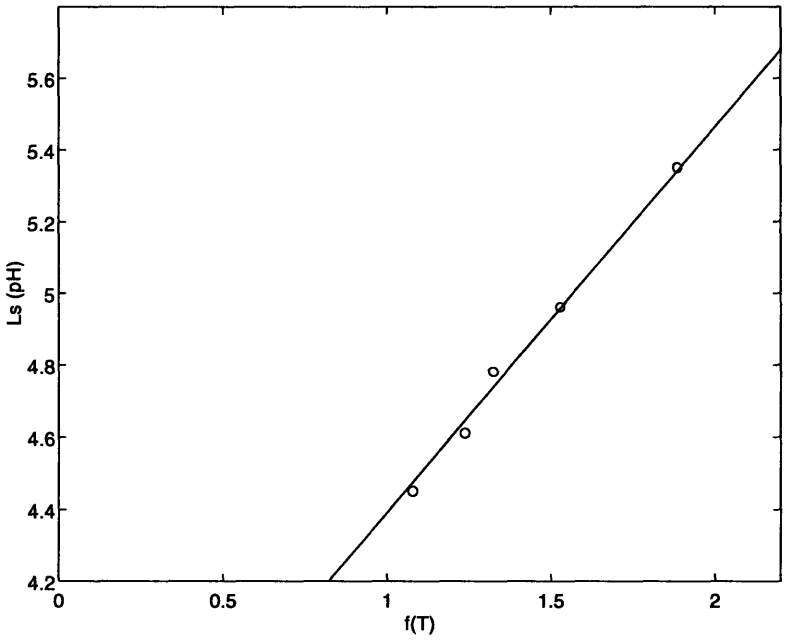

Figure 3-9: Self-inductance measurements for array on a ground plane. The inductance is plotted versus $f(T) = 1/[1-(T/T_c)^4] = \lambda^2/\lambda_o^2$. The solid line represents the model, and requires $h = 505\,\text{nm}$ and $\lambda_o = 89.5\,\text{nm}$.

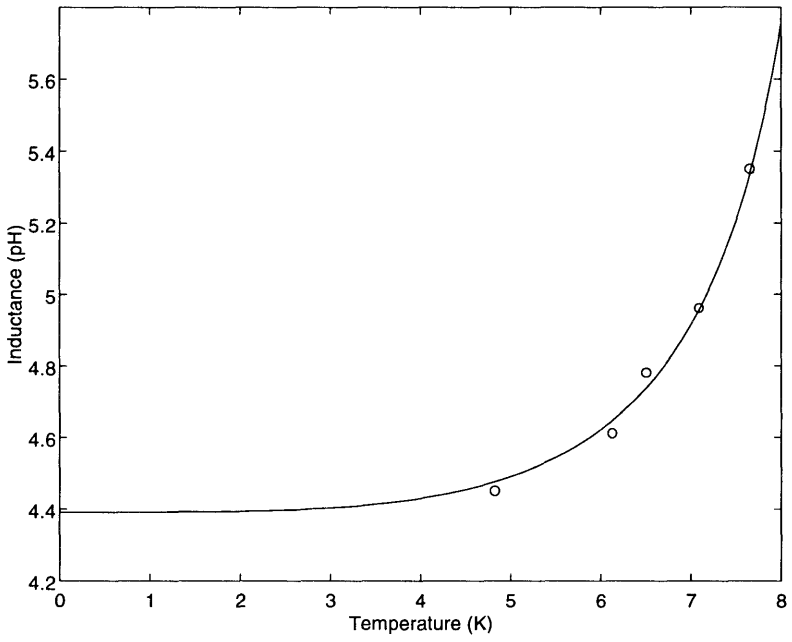

Figure 3-10: Self-inductance measurements for array on ground plane. The solid line represents the model.

We can again use a simple model to calculate the inductive coupling between a loop of our circuit and the control wire providing a magnetic field. As sketched in Fig. 3-11, the control wire is treated as an infinite and infinitely thin perfectly conducting line. The ground plane is treated as an infinite, perfectly conducting plane with a skin depth, $\lambda(T)$. The loop is also comprised of thin wires. Calculation of the inductance gives

$$M^{\text{eff}} = \frac{\mu_o p}{4\pi}\left[\ln\left(\frac{p^2+d^2}{d^2}\right) - \ln\left(\frac{p^2+(d+h+\lambda(T))^2}{(d+h+\lambda(T))^2}\right)\right] \tag{3.9}$$

Fig. 3-12 shows that this provides a good estimate for the magnitude of the inductive coupling, M_{ctrl}, but does not sufficiently account for the influence of changing temperature.

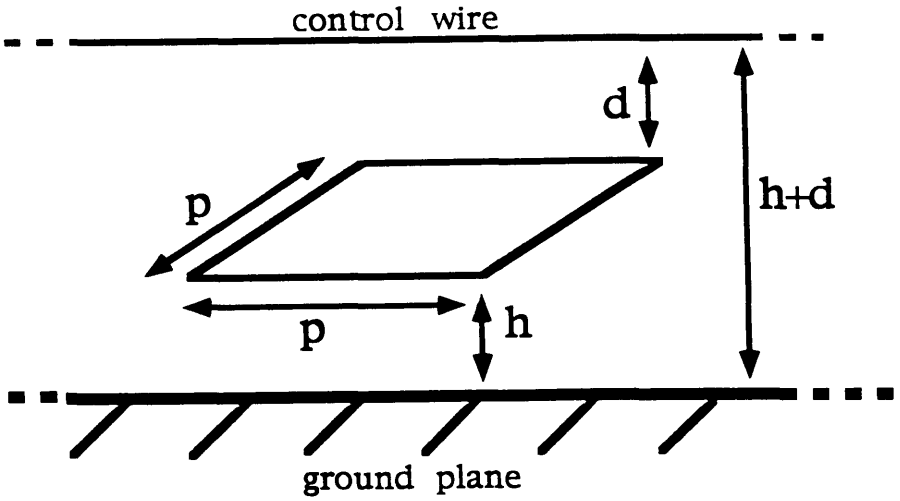

Figure 3-11: Geometric configuration for modeling the control line inductance.

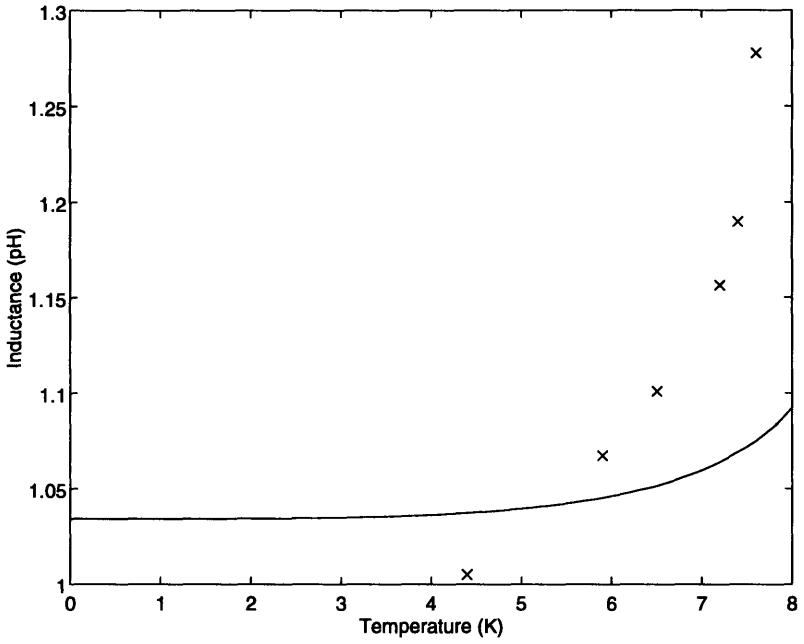

Figure 3-12: Control line inductance versus temperature. The solid line represents the model.

The change in L_s has a clear effect on the transistor characteristics of the device. Equation (1) predicts that V_E will double for $L_s^{\text{eff}} = L_s/4$. This is almost exactly what we observe, as shown in Fig. 3-13. The period of V_E has increased by a factor of about four, which corresponds to the decreased effective coupling, $M_{\text{ctrl}}/4$. The transresistance, which is proportional to $M_{\text{ctrl}}/\sqrt{L_s}$, is half as large as before.

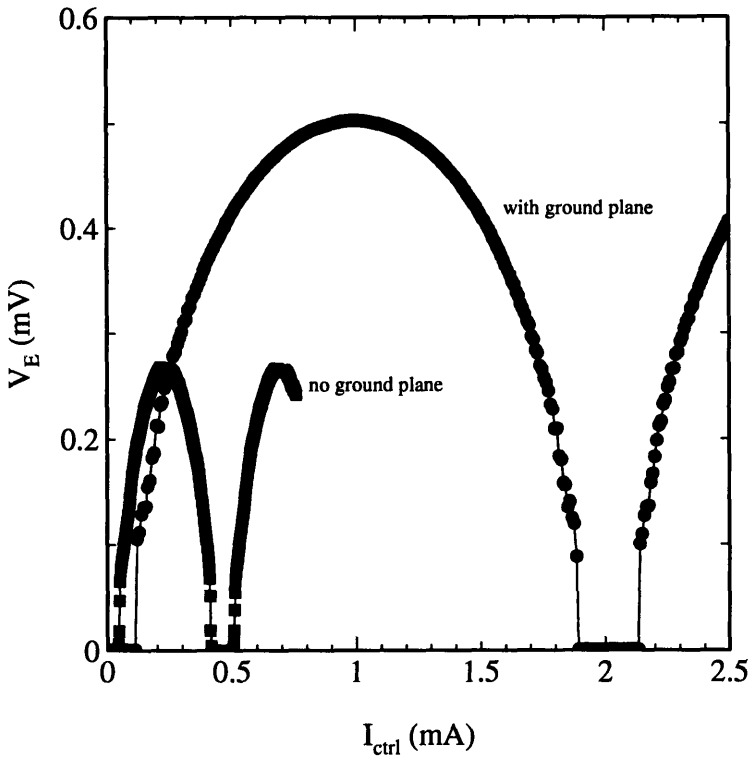

Figure 3-13: IV characteristic of 54-junction arrays at $T = 4.2\,K$ and constant I_b.

The higher output voltage levels also improve the performance of the oscillator. The bandwidth is twice as large, and the maximum power has more than doubled. This is because the current levels are also much higher, as seen in the $V(I_b)$ characteristics of Fig. 3-14. Here, the curves for several different control current values are presented. (Note that data points after the switch to the gap voltage are not included). Near V_E, the slopes become quite steep, and the decreased r_0 gives much narrower linewidths.

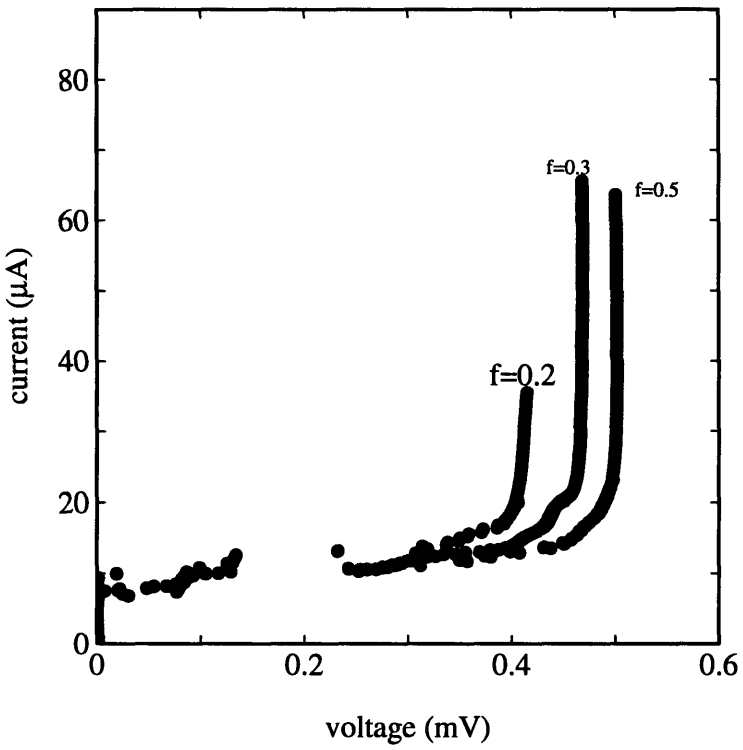

Figure 3-14: IV characteristic of 54-junction arrays at $T = 4.2\,K$ and several different values of I_{ctrl} (or f).

The presence of a superconducting ground plane reduces all inductance values and introduces a temperature dependencs to the inductances. The presence of the superconducting ground plane improves all of the Measurements of the devices show steeper Eck steps at higher voltage and current levels. As a result, all of the device parameters except the transresistance are improved, indicating that a ground plane should only be used for oscillator applications. We have successfully modeled these trends in our data, and we can use this knowledge to further optimize the device performance.

Device Parameters

Parameter	Single Array no gnd-plane	Single Array on gnd-plane	Coupled Arrays on gnd-plane
$V_{E,max}$ (mV)	0.27	0.5	0.91
r_m (Ω)	1.75	0.53	1.5
r_0 (Ω)	0.62	<0.1	3.3
I_{th} (mA)	0.05	0.09	0.1
I_{per} (mA)	0.45	2.0	2.0
B (GHz)	130	240	240
P (nW)	8	35	29

Table 3.2: Device Parameters, T=4.2 K

3.5 Inductively Coupled Arrays

Additional output voltage is obtained by connecting two arrays of 54 Josephson junctions in series. The control wire is now placed along both edges of the device and is again 500 nm above it. Voltage leads at the edge of the arrays make it possible to measure the voltage across both rows or across a single row. This structure is illustrated in Fig. 3-15.

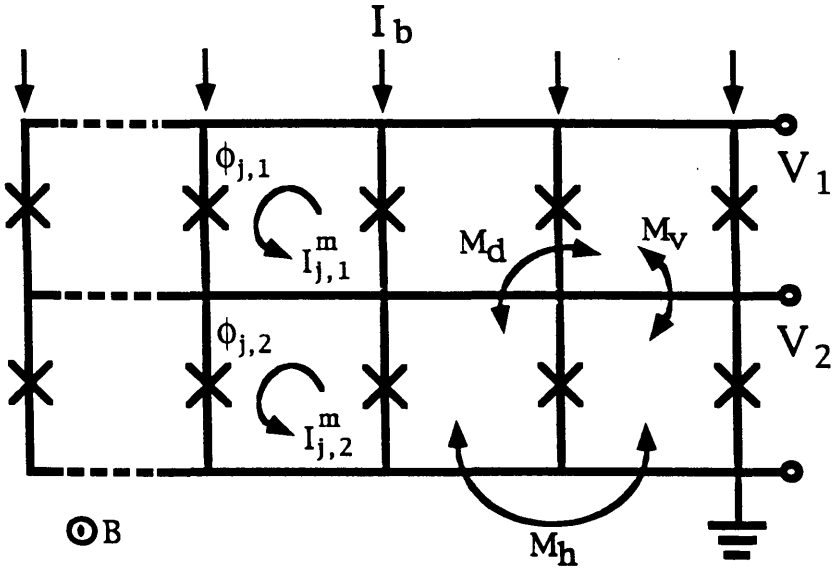

Figure 3-15: Circuit diagram of the inductively coupled array.

As discussed in section 2.3.2, we expect to see two Eck steps due to the inductive coupling. The perturbation analysis predicts

$$V_{E\pm} = \frac{\Phi_o}{\pi\sqrt{L_s C}} |\sin(\pi f)| [1 + (|M_h + M_d|)\cos(2\pi f) \pm \frac{1}{2}|M_v|] \tag{3.10}$$

where V_{E+} corresponds to in-phase oscillations of the rows and V_{E-} corresponds to out-of-phase oscillations.

Measurements confirm that there are two resonant modes in the system. Fig. 3-16 shows the voltage across each row of a 54x2 array when current is uniformly injected. Two steps clearly appear in the iv when the voltage is measured across a single row. Across both

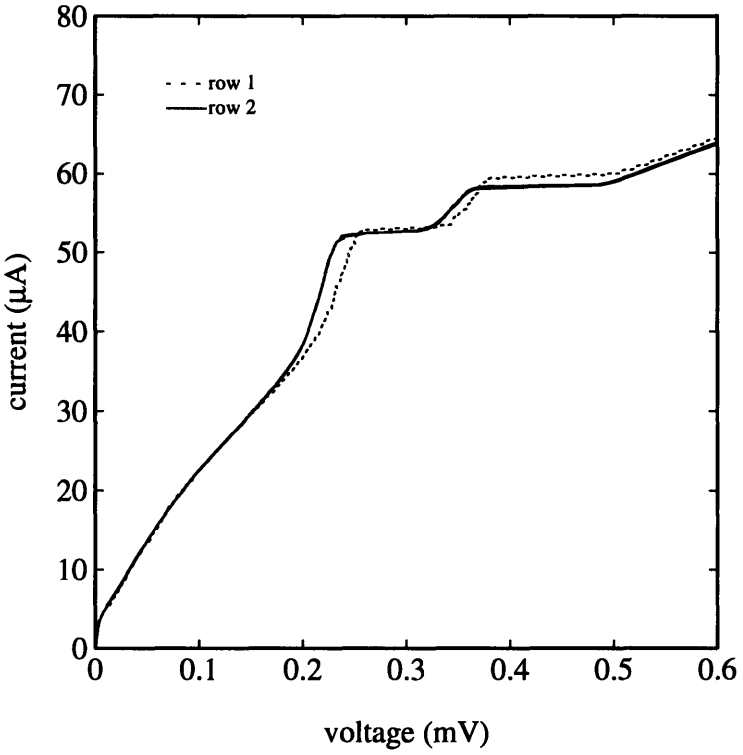

Figure 3-16: Measurements of an inductively coupled array, N=54x2, on a ground plane. The solid curve represents the voltage measured across the top row, while the dotted line is the voltage across the bottom row. The measurements are taken at $7.2\,K$ and $f = 0.1$.

rows, we again see the two steps at twice the voltage, Fig. 3-17. The steps across both rows are not as sharp, since the voltages across each row are not quite the same, as shown in Fig. 3-16. In Fig. 3-18, we plot the voltage positions of the steps versus frustration. The model seems to work best near $f = 0.5$. As expected, the values of M_h and M_v are approximately the same, while M_d is about half as large.

At low temperatures, the experimental results are somewhat more perplexing. Fig. 3-19 shows the iv curves at 4.2K for several different values of the frustration. The size of the splitting is significantly smaller, indicating that the coupling ratio, M_v decreases with temperature for devices on a ground plane. As the current is steadily increased, a step first

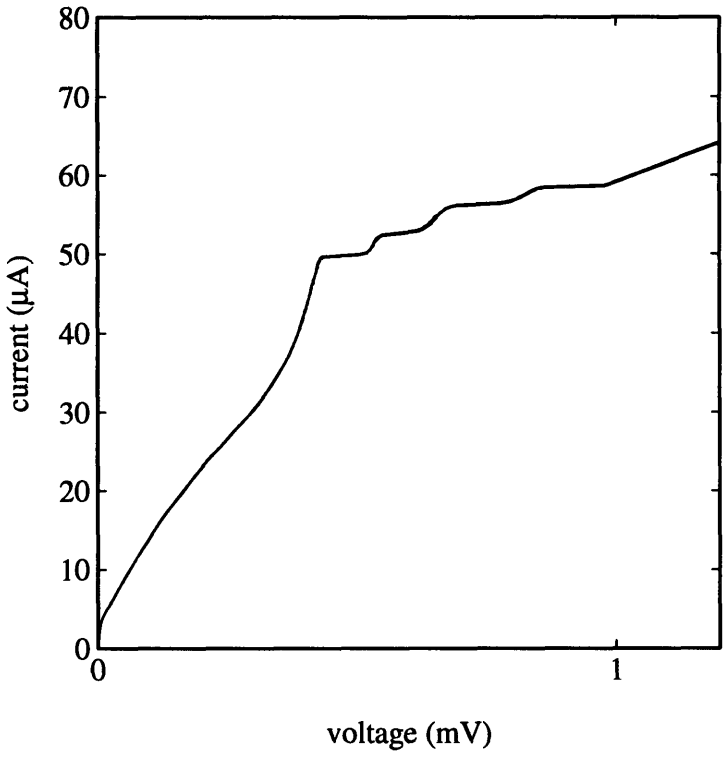

Figure 3-17: Measurements of an inductively coupled array, N=54x2, on a ground plane. The voltage is measured across both rows at 7.2 K and $f = 0.1$.

appears at V_{E+}. Continuing to increase the current, the voltage makes a jump to V_{E-}. This behavior was not seen in either simulations or measurements of shorter inductively coupled arrays (N=9x2). We are still investigating the possibility that it is an experimental artifact.

The presence of two characteristic frequencies in this system makes it attractive for device applications. As an oscillator, the device has two possible frequencies. However, the power that can be coupled from the device is expected to be different for each mode. In the anti-symmetric mode, the voltage amplitudes of the small oscillations are out of phase. Thus, the corresponding superposed AC electric fields should give no power output. In the symmetric mode, the small oscillations are in phase. In this case, the AC electric fields add, and the amplitude is expected to be large at resonance. As in the single array, the

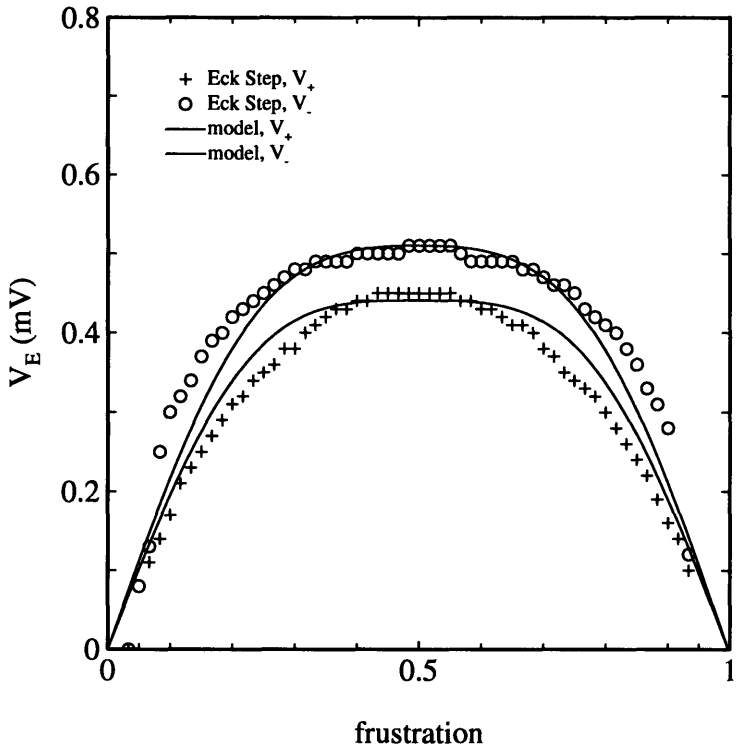

Figure 3-18: The measured voltages of both steps versus frustration, for an array of N=54x2. This data was taken across one row of an array, at $T = 7.0\,K$. The solid line shows the fitted model, with $M_v = 0.12$ and $M_h + M_d = 0.18$.

frequencies can be tuned with a control current and are stable for a relatively wide range of bias currents. The bandwidth is approximately the same as for the single array. The power decreases slightly due to a decrease in I_E. A large rise in the output resistance causes the linewidth, given by equation 3.6, to increase. However, this expression for the linewidth was derived from the thermal fluctuations in a resistive element. It is not clear, yet, whether phase locking between the two rows acts to reduce the linewidth.

At low temperatures, where the splitting is negligible, the array can be used as a transistor. The output voltage is twice that of a single array. Differences in the transfer characteristics of all three devices can be seen clearly in Fig. 3-20, where their transistor

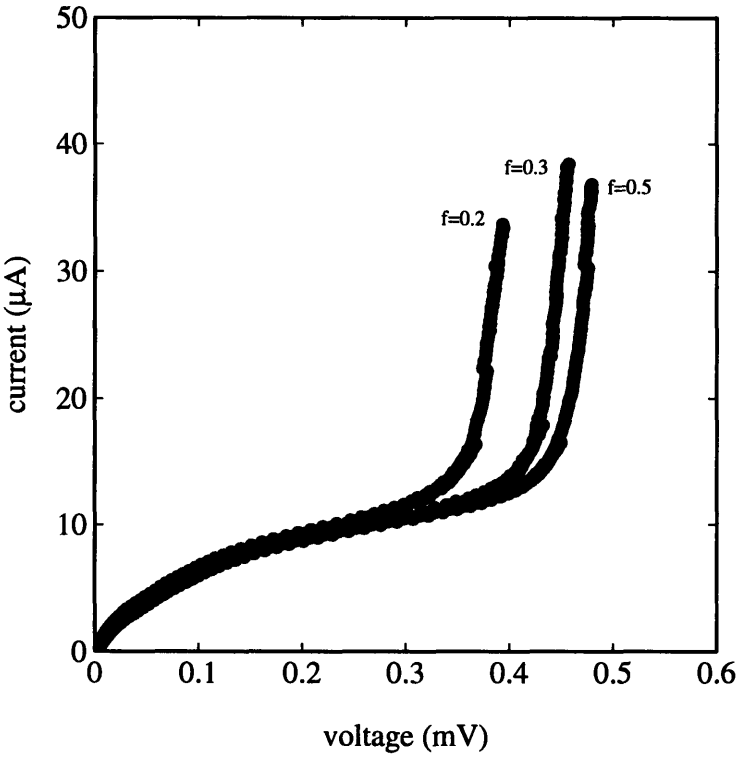

Figure 3-19: Measurements of an N=54x2 array above a ground plane, at $T = 4.2\,K$.

curves are presented. The currents are normalized to I_{per}, the values of which are given in Table I. The period of the coupled arrays is the same as that of the single array on the ground-plane. Since the output voltages are larger, r_m increases.

Use of the inductively coupled devices depends on further devolopment of our models. However, the match between the theory and measurements is not as good as in our previous devices, and more work is needed to fully understand the dynamics of this system.

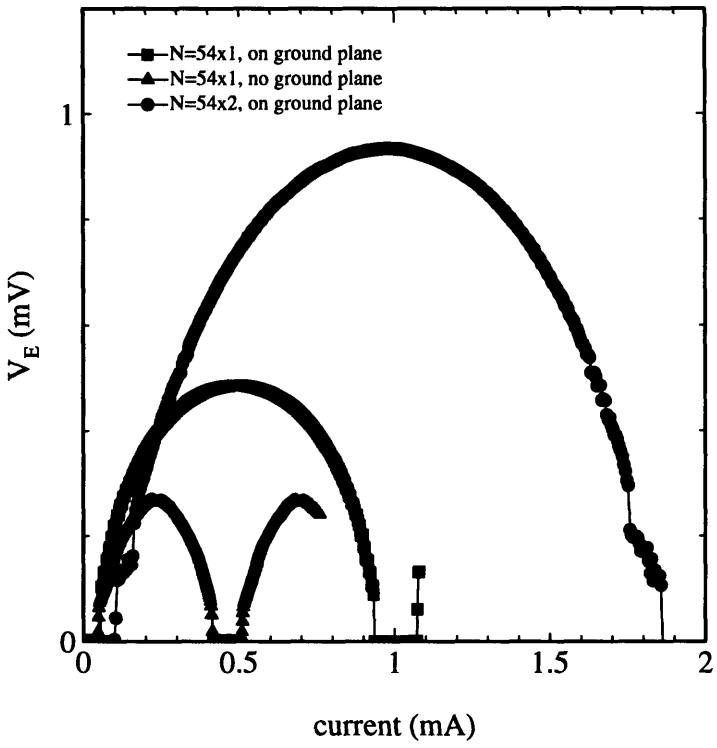

Figure 3-20: Transistor measurements of the N=54x1 arrays, on and off the ground plane, and of the N=54x2 array.

Chapter 4

Conclusions

4.1 Summary

We have measured the device characteristics of arrays of underdamped Josephson junctions connected in parallel. We demonstrated that it is possible to model the performance of these devices and thus optimize their parameters for specific applications. Our models indicate that study of these systems may also lead to important insights on the motion of soltions in discrete lattices.

We were able to enhance device performance by manipulating the inductances of single arrays. We used a superconducting ground plane to lower the inductance values, which improved all of the parameters except the transresistance. Thus the ground plane should be used in the design of oscillators and should be omitted when the array is to be used as a transistor. Our models suggest that the devices can also be improved by using smaller junctions or junctions with lower capacitances.

We attempted to further refine the devices by connecting two arrays in series. This configuration achieved higher voltage levels and transresistances, but the output resistance was degraded. The power and bandwidth were relatively unaffected. We also observed a splitting of the flux-flow step, due to magnetic coupling in the system. The splitting was predicted mathematically and compared with our measurements.

4.2 Continuing and Future Work

The dynamics of inductively coupled arrays must be more carefully studied before their potential as devices can be fully realized. We have already observed splitting of the resonant steps in smaller arrays, and are currently investigating these systems. We are also interested in characterizing the effects of temperature on the mode splitting and relative stability.

A complete characterization of the oscillator performance must include AC measurements. A particularly important parameter is the linewidth of the output radiation. It has been suggested that the linewidth in inductively coupled arrays may be decreased by phase locking effects, although no measurements are yet available to confirm this. It will also be necessary to compare the AC power output of a single array, with and without a ground plane, to that of each mode in the inductively coupled system.

Appendix A

Calculation of Critical Field

We want to determine the value of the applied magnetic field at which it becomes energetically favorable for a vortex to exist in the system. Consider, then, two states of the system: an array with a vortex and an array with no vortex. It is possible to have a transition between the states when they are in equilibrium. By definition, the total entropy of the two states is maximized in equilibrium. This implies that the Gibbs Free energies must be equal. We will therefore obtain expressions for the Gibbs free energy of each state.

The transition between a vortex and a no-vortex state occurs without generation of heat, and is called a second-order phase transition. This fact simplifies the expression of the Gibbs free energy to [15]

$$G(\vec{H},T) = G(0,T) - \tilde{W} \tag{A.1}$$

where $G(0,T)$ is the Gibbs free energy in the absence of applied electromagnetic fields, and $\tilde{W}$ is the co-energy of the system. Define the two states:

$$\begin{aligned} G^1(\vec{H},T) &= \text{ array with vortex present} \\ G^0(\vec{H},T) &= \text{ array without vortex} \end{aligned} \tag{A.2}$$

then:

$$G^1(\vec{H},T) = G^1(0,T) - \tilde{W}^1 \tag{A.3}$$

$$G^0(\vec{H},T) = G^0(0,T) - \tilde{W}^0 \tag{A.4}$$

If we assume that $G^1(0,T) \approx G^0(0,T)$, then

$$G^1(\vec{H},T) - G^0(\vec{H},T) = \tilde{W}^0 - \tilde{W}^1 \tag{A.5}$$

Therefore, $G^1 = G^0$ when $\tilde{W}^1 = \tilde{W}^0$. If we assume that the system is linear, we can simply calculate the electromagnetic energies of the two states. When these are equal, we will say that it is energetically favorable for a vortex to exist in the system.

The electromagnetic energy is calculated in terms of circuit variables of the system. This approach is correct if two additional assumptions are allowed: (1) that, on an arbitrary surface surrounding the circuit, the fields are electro-quasi-static, and (2) that, on this surface, $\partial D/\partial t \rightarrow 0$ [31]. Then the total electomagnetic energy is:

$$dw = v\,dq + i\,d\Phi \tag{A.6}$$

In section 2.3.1, the result for a single junction is given:

$$W = \frac{\Phi_o I_c}{2\pi}(1 - \cos\phi_j) + \frac{L_s}{2}(I_j^m)^2 \tag{A.7}$$

For the simple case of self-inductance only,

$$I_j^m = \frac{\Phi_o}{2\pi L_s}(\phi_j - \phi_{j+1} - 2\pi f) \tag{A.8}$$

Then, for the entire array,

$$W = E_J \sum_{i=1}^{N}(1 - \cos\phi_i) + \frac{E_J L_J}{2L_s}\sum_{i=1}^{N-1}(\phi_{i+1} - \phi_i - 2\pi f)^2 \tag{A.9}$$

where

$$E_J = \frac{\Phi_o I_c}{2\pi} \tag{A.10}$$

The static solutions for ϕ discussed in section 2.3.1 can now be used to find the electromagnetic energy as a function of frustration. We plot $W^0(f)$ and $W^1(f)$ for given values of E_J and L_s. The point at which the energies of the two states are equal defines the phase transition, and is called the critical frustration, f_{c1}.

Appendix B

Long Josephson Junction Model

Long Josephson junctions are characterized by lengths much larger than the magnetic field penetration depth, λ_J. Since these systems have been studied extensively, it is useful to compare their behavior and parameters with those of the discrete arrays. We will focus on those parameters which are used for diagnostics in our discrete arrays.

We are primarily interested in the slope and intercept of the linear fit shown in Fig. 3-4. This is because Owen and Scalapino [29] have done analytical calculations relating these parameters to the Josephson penetration depth and the thermodynamic critical field. They found that, while the junction is still in the Meissner state, the maximum critical current is given by

$$I_{\max} = \frac{wc}{2\pi}(H_o - |H_e|) \tag{B.1}$$

H_e is the externally applied field, and H_o is the maximum value of the external field for which the Meissner solution is valid. Converting H and I to MKSA, and normalizing the current, we obtain

$$\frac{I_{\max}}{I_c(0)} = \frac{2w}{I_c(0)}(H_o - |H_e|) \tag{B.2}$$

Fig. B-1 compares the dimensions of the long junction with the parallel array, and Table B.1 gives the approximations that we will use to convert from one system to the other. To use the results of Owen and Scalapino on a discrete system, we write $w \rightarrow p$ and

$I_c(0) \rightarrow NIc(0)$. Then equation B.2 becomes

$$\frac{I_{\max}}{NI_c} = \frac{2p}{NI_c}(H_o - |H_e|) \tag{B.3}$$

The field is converted to frustration by $\Phi_o = Bp^2$.

$$\frac{I_{\max}}{NI_c} = \frac{2\Phi_o}{\mu_o pNI_c}(f_o - f) \tag{B.4}$$

We now replace the quantity $\Phi_o/2\pi I_c$ by the Josephson inductance, L_J, and approximate that $L_s \approx \mu_o p$. Finally, the normalized current measured in a discrete system is

$$\frac{I_{\max}}{NI_c} = \left(\frac{L_J}{L_s}\right)\left(\frac{4\pi}{N}\right)(f_o - f) \tag{B.5}$$

In discrete arrays, we measure the maximum critical current in the region near $f = 0$ (while the system is still in the Meissner state). For this measurement, current is injected at the edge of the array, imitating the current injection in long junctions. The slope of the linear region in Fig. 3-4 gives us an estimate of the inductance ratio, L_J/L_s. The intercept, f_o, is the field value at which the Meissner solution is no longer valid. It has been shown that this field is related to the critical field value, f_{c1}, at which the presence of a vortex in the system is thermodynamically favored [30]. The two fields are different by a factor of $2/\pi$, and are given in Table B.1. In Fig. 2-8, we compare this estimate of f_{c1} with simulations of our discrete system to demonstrate the efficacy of the long Josephson junction model.

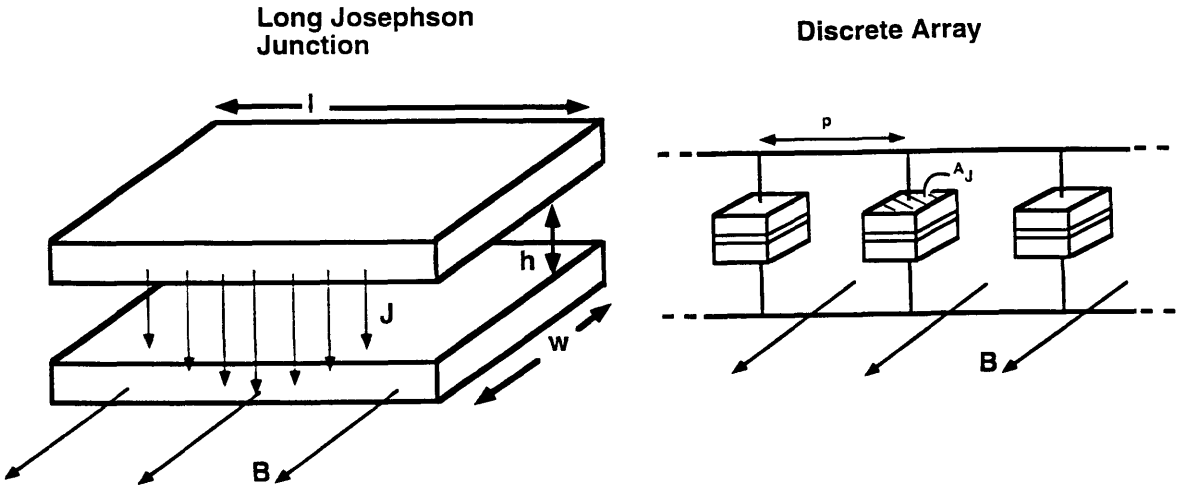

Figure B-1: Dimensions of the Long Josephson Junction versus the Discrete Array.

Long Junction	Parallel Array
h	p
w	p
λ_J	Λ_Jp
$I_c(0)$	$NI_c(0)$
$\alpha = \frac{2w}{I_c(0)}$	$\alpha = \frac{L_J}{L_s}\frac{4\pi}{N}$
$H_o = \frac{\Phi_o}{\pi\lambda_J h\mu_o}$	$f_o = \frac{1}{\pi\Lambda_J}$
$H_{c1} = \frac{2\Phi_o}{\pi^2\lambda_J h\mu_o}$	$f_{c1} = \frac{2}{\pi^2\Lambda_J}$

Table B.1: Conversion table for dimensions and parameters.

Appendix C

Publications

Discrete Underdamped Vortex Flow Devices

A. E. Duwel, H. S. J. van der Zant, T. P. Orlando
Massachusetts Institute of Technology, Cambridge, MA 02139

Abstract— **Vortex flow devices consisting of discrete arrays of underdamped Josephson junctions have been fabricated and measured. These devices and their long, continuous junction counterparts are based on the ability to magnetically control the Eck voltage in an underdamped system. We find that both transistor and oscillator parameters are improved by placing the arrays above a superconducting ground plane and by connecting two arrays in series. We developed models for the device behavior which numerically numerically account for the measured parameters. Our models also suggest that junctions with smaller capacitances will further improve the device parameters.**

I. Introduction

Parallel arrays of Josephson junctions behave, in many ways, like long, continuous junctions. Both structures may be used as superconducting circuit elements, such as transistors, oscillators, phase shifters, and amplifiers. These systems also serve as valuable models for high temperature superconducting devices.

Josephson junctions can be designed to operate in two different regimes. These are distinguished by the value of the McCumber parameter, β_c. Overdamped junctions, where $\beta_c < 1$, have been studied and function well as superconducting transistors. Transistors made from long, overdamped junctions have shown gains of about 10 and transresistances of about $0.2\,\Omega$ [1], [2]. Parallel arrays of Josephson junctions have been fabricated with gains of about 1.2 and transresistances of $0.43\,\Omega$ [3].

Although underdamped junctions ($\beta_c > 1$) exhibit more complicated dynamics, they also offer promising device characteristics. Long, underdamped junctions have been designed as transistors and as oscillators. Transresistances of the order of $0.01\,\Omega$ [4] and available output power levels of about 20 nW at 260 GHz [5] have been achieved. However, the output impedence levels are less than $1\,\Omega$. Parallel arrays of underdamped junctions compete with these devices, operating with transresistances of about $1.8\,\Omega$, expected power levels of about 10 nW, and output impedences of the order of $10\,\Omega$ [6]. In this paper, we discuss the operation of the underdamped array as a vortex flow device and present simple models for its output parameters. We have also measured two variations on the underdamped array, and we show that, in both systems, the device parameters are improved.

Manuscript received October 16, 1994.

A. E. Duwel, e-mail duwel@mit.edu.

This work was conducted under the auspices of the Consortium for Superconducting Electronics with the partial support of the Advanced Research Projects Agency (MDA 972-90-C-0021) and National Science Foundation Graduate Research Fellowships.

II. Samples

Samples were fabricated with a Nb trilayer process. [1] All of the devices which we discuss are on the same chip, and their physical parameters are measured at a temperature of 4.2 K. Each Josephson junction has an area of $8\,\mu m^2$ and a capacitance, C, of 300 fF. We measured the normal-state resistance, R_n, to be about $275\,\Omega$. Taking the I_cR_n product to be 1.75 mV at 4.2 K, we find that the critical current, $I_c = 6.4\ \mu A$. This gives a value for the Josephson inductance, $L_J = \Phi_0/2\pi I_c$, of 51 pH. The McCumber parameter, $\beta_c = R_n^2C/\,L_J$, is about 445 at 4.2 K, indicating that the junctions are highly underdamped.

Each of the devices on the chip can be subjected to a magnetic field through coupling to a superconducting control wire. The amount of magnetic flux supplied to the device, Φ_{app}, depends on the strength of the mutual inductive coupling, M_{ctrl}, and can be written as

$$\Phi_{app} = \frac{I_{ctrl}M_{ctrl}}{\Phi_0} \qquad (1)$$

where I_{ctrl} is the amount of current in the control wire, and we have normalized the applied flux to one flux quantum, Φ_0.

III. Underdamped Vortex Flow Device

Figure 1 shows a schematic of the vortex flow device, which consists of 54 Josephson junctions, connected in parallel by superconducting Nb wires. A bias current, I_b, is applied uniformly to each junction, and the voltage is measured with superconducting leads at one end of the array. The control current providing a magnetic field runs

[1] Hypres, Inc. Elmsford, NY 10523

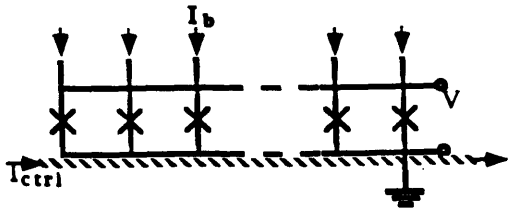

Fig. 1. *A schematic drawing of the vortex flow device.*

parallel to the edge of the array and is about 500 nm above it.

The magnetic field from $I_{\rm ctrl}$ injects vortices into the array. The bias current causes the vortices to move, thereby producing a voltage across the array, V, proportional to the vortex velocity. For a fixed $I_{\rm ctrl}$, increasing I_b causes an increase in velocity, until the limiting electromagnetic phase velocity in the array is reached. At this point, increasing I_b further does not move the voltage beyond V_E, the Eck voltage [7]. Thus there is a steep rise in the current, as shown in Fig. 2. For sufficiently high I_b, the voltage jumps to the gap voltage, V_g.

When I_b is held constant and $I_{\rm ctrl}$ is increased, V_E initially increases due to the higher density of injected vortices. However, as the inset shows, V_E is periodic in $I_{\rm ctrl}$, with period $I_{\rm per}$, which reflects the fact that the properties of an array are periodic in magnetic field. The lighter line in the inset is the result of a linear analysis for V_E [6] and is given by

$$V_E = \frac{\Phi_0}{\pi\sqrt{L_s C}}\left|\sin\left(\frac{\pi\Phi_{\rm app}}{N-1}\right)\right| \qquad (2)$$

where L_s is the self inductance of a single loop (cell) in the array, and $N-1$ is the number of cells in the array. The value of L_s is determined from the diagnostic methods described in reference [8]. For this sample, L_s is 16 pH.

From equations (1) and (2), we see that the array may be used as a current-controlled voltage source. The device is biased at I_b, with input current I_{ctrl} and output voltage V_E. The maximum output voltage is inversely proportional to $\sqrt{L_s C}$ and the transresistance, $r_m = \partial V_E/\partial I_{\rm ctrl}$, increases as $M_{\rm ctrl}/\sqrt{L_s C}$ increases. The transresistance depends on the operating point and can be obtained graphically by taking the slope of the tangent to the $V_E(I_{\rm ctrl})$ curve. For $V_E \approx 0.75 V_{\rm E,max}$, we obtain $r_m = 1.75\,\Omega$. The threshold current, discussed in detail in reference [6], can be modeled simply as: $I_{\rm th} = 3.6 I_c\sqrt{L_J/L_s}$. For this device, we have $I_{\rm th} = 0.05$ mA, which matches the theory well. The output resistance, r_0, is given by the slope of $V(I_b)$ as the voltage approaches V_E. This parameter affects the operating range of the transistor and should be as small as possible.

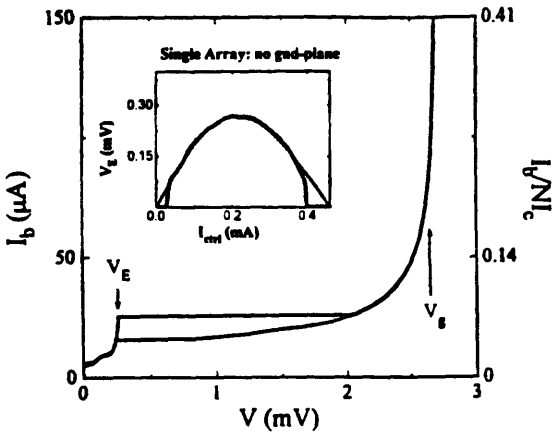

Fig. 2. *Current vs. voltage curves of Josephson junction array at 4.2K. V_E is the Eck voltage and V_g is the gap voltage. The inset figure compares the transistor characteristic to theory.*

This underdamped array may also be used as a current-controlled oscillator. The control current determines V_E, which, according to the Josephson relation, corresponds to a frequency, $\nu = V_E/\Phi_0$. For our device, V_E ranges from 0 to 0.27 mV, giving a bandwidth of 130 GHz. Based on the linewidth of a single junction oscillator [6], [9], we expect the array linewidth to be proportional to r_0. The output impedence can be estimated by modeling the junction array as a transmission line, giving $Z_0 = \sqrt{L_s/C} \approx 10\,\Omega$. The maximum attainable power, $P = V_{\rm E,max} I_{E,max}$, is about 8 nW. A summary of these device parameters is given in Table I.

Our simple models suggest that we can improve the output voltage and maximum power by decreasing L_s and C. We also expect higher voltages and possibly smaller linewidths from two arrays connected in series. In the following sections, we discuss configurations which address both of these issues.

TABLE I
DEVICE PARAMETERS (T=4.2K)

Parameter	Single Array no gnd-plane	Single Array on gnd-plane	Coupled Arrays on gnd-plane
$V_{\rm E,max}$ (mV)	0.27	0.5	0.91
r_m (Ω)	1.75	0.53	1.5
r_0 (Ω)	0.62	<0.1	3.3
$I_{\rm th}$ (mA)	0.05	0.09	0.1
$I_{\rm per}$ (mA)	0.45	2.0	2.0
B (GHz)	130	240	240
P (nW)	8	35	29

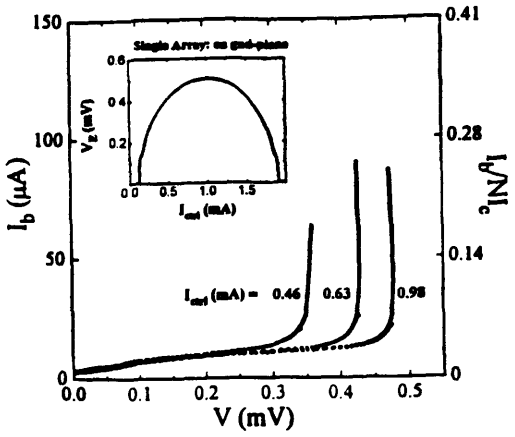

Fig. 3. *Current vs. voltage curves of Josephson junction array above a superconducting ground plane. Measurements are at 4.2K and various I_{ctrl}. The inset figure shows the I-V for the device when biased as a transistor.*

IV. Devices on Ground Plane

In order to lower L_s, we placed the same array of Josephson junctions about 200 nm above a superconducting ground plane. Our diagnostic measurements indicate that the effective inductance in the presence of a ground plane, L_{eff}, is lower than L_s by a factor of about four.

This change in L_s has a clear effect on the transistor characteristics of the device. Equation (1) predicts that V_E will double for $L_{eff} = L_s/4$. This is almost exactly what we observe, as shown in the inset of Fig. 3. As expected, I_{th} is also approximately twice as large. The period of V_E has increased by a factor of about four, which corresponds to a decreased effective coupling, $M_{eff} = M_{ctrl}/4$. The transresistance, which is proportional to $M_{ctrl}/\sqrt{L_s}$, is half as large as before. We can quantitatively account for the smaller mutual and self-inductances by modeling the control line as an infinitely long wire, each cell of the array as a square loop, and the ground plane as an infinite, perfectly conducting sheet.

The higher output voltage levels also improve the performance of the oscillator. The bandwidth is twice as large, and the maximum power has more than doubled. This is because the current levels are also much higher, as seen in the $V(I_b)$ characteristics of Fig. 3. Here, the curves for several different control current values are presented. (Note that data points after the switch to the gap voltage are not included). Near V_E, the slopes become quite steep, and the decreased r_0 gives narrower linewidths.

The presence of the superconducting ground plane improves all of the device parameters except the transresistance. We have successfully modeled these trends in our data, and we can use this knowledge to further optimize the device performance.

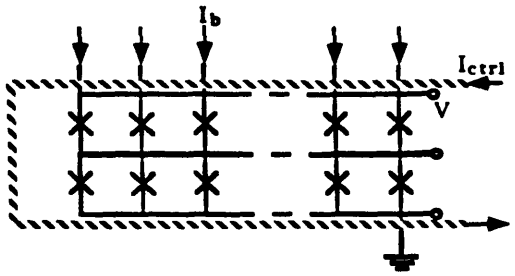

Fig. 4. *Schematic of two arrays connected in series.*

V. Coupled Device on Ground Plane

Additional output voltage is obtained by connecting two arrays of 54 Josephson junctions in series. The control wire is now placed along both edges of the device and is again 500 nm above it. This structure also lies above a superconducting ground plane and is illustrated in Fig. 4.

At 4.2 K, the $V(I_b)$ curves for this device look similar to the single array on the ground plane. However, there is a much more gradual rise in the current near V_E, resulting in higher output resistances. The voltage across the coupled arrays is twice that of the single array, which is the expected result of placing two equal voltages in series.

Differences in the transfer characteristics of all three devices can be seen clearly in Fig. 5, where their transistor curves are presented. The currents are normalized to I_{per}, the values of which are given in Table I. The period of the coupled arrays is the same as that of the single array on the ground-plane. Since the output voltages are larger, r_m increases.

Despite the higher voltage levels, the frequency of the Josephson oscillations does not change, and the bandwidth is the same. The power decreases slightly due to a decrease in I_E. The large rise in the output resistance causes the linewidth to increase. This change in r_0 implies that these arrays are dynamically more complex than our previous structures.

Inductively coupled arrays are the discrete version of long, continuous stacked Josephson junctions. In the stacked junctions, two Eck voltages have been predicted and observed [10]–[12], corresponding to two limiting electromagnetic phase velocities. A simple analysis of the discrete system predicts

$$V_{E1,E2} = \frac{\Phi_0}{\pi\sqrt{L_s C}}\left|\sin\left(\frac{\pi\Phi_{app}}{N-1}\right)\right|[1 \pm M] \qquad (3)$$

where M is the strength of the coupling between adjacent cells of the two arrays, and we have neglected other coupling effects for simplicity. The result is that there are now two modes of oscillation. In the antisymmetric mode, the corresponding junctions in each row oscillate

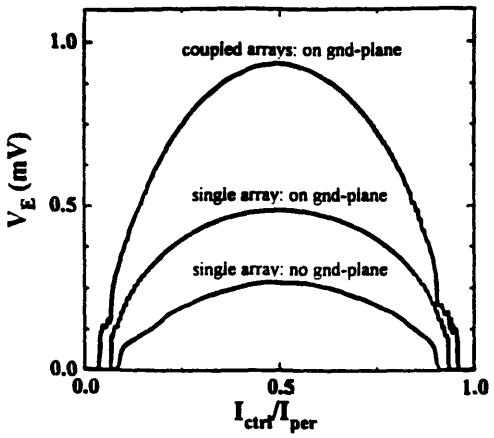

Fig. 5. *Transistor characteristics of each device at 4.2 K. The currents are scaled to the current interval of one period, I_{per}.*

with equal amplitude but out of phase, and the characteristic frequency (or voltage, V_{E1}) is higher than in the single array. In the symmetric mode, the rows oscillate in phase, and the characteristic frequency is lower.

Two voltages are visible in our $V(I_b)$ curves at temperatures above about 6 K, but do not appear at 4.2 K. Fitting equation (3) to data taken at 7.2 K required that $M \approx 0.5L_s$. Based on measurements of the nearest-neighbor coupling in a single array [8], this value is higher than we expected. By including other nearest-neighbor inductances, the value of M used in the fits is lowered. However, the match between the theory and measurements is not as good as in our previous devices, and more work is needed to fully understand the dynamics of this system.

VI. Conclusion

We have measured the device characteristics of arrays of underdamped Josephson junctions connected in parallel. We demonstrated that it is possible to model the performance of these devices and thus optimize their parameters for specific applications. This was achieved by manipulating the inductances of single arrays. We used a superconducting ground plane to lower the inductance values, which improved all of the parameters except the transresistance. It is clear from our models that the devices can also be improved by using smaller junctions or junctions with lower capacitances. In addition to optimizing the device parameters, a study of the noise performance of these devices must still be conducted.

We attempted to further refine the device parameters by connecting two arrays in series. This configuration achieved higher voltage levels and transresistances, but the output resistance was degraded. The power and bandwidth were relatively unaffected. These inductively coupled arrays may be promising for some applications, but the dynamics must be more carefully studied before this potential can be realized.

Acknowledgment

We thank Enrique Trias and Joel Phillips for valuable discussions.

References

[1] D. P. McGinnis, J. B. Beyer, and J. E. Nordman, "A Modified Superconducting Current Injection Transistor and Distributed Amplifier Design," *IEEE Trans. Mag.*, vol. 25, pp. 1262–1265, March 1989.

[2] B. J. Van Zeghbroeck, "Superconducting Current Injection Transistor", *Appl. Phys. Lett.*, vol. 42 (8), pp. 736–738, April 1983.

[3] D. Berman, H. S. J. van der Zant, and T. P. Orlando, "Discrete Superconducting Vortex Flow Transistors," *IEEE Trans. Appl. Superconductivity*, vol. 4, pp. 161–168, September 1994.

[4] D. P. McGinnis, J. E. Nordman, and J. B. Beyer, "Optimization of Circuit Parameters for the Vortex Flow Transistor," *IEEE Trans. Mag.*, vol. 23, pp. 699–702, March, 1987.

[5] Y. M. Zhang, D. Winkler, and T. Claeson, "Detection of MM and SUBMM Wave Radiation from Soliton and Flux-Flow Modes in a Long Josephson Junction," *IEEE Trans. Appl. Superconductivity*, vol. 3 (1), pp. 2520–2523, March, 1993.

[6] H. S. J. van der Zant and T. P. Orlando, "The Eck Peak in Underdamped Discrete Superconducting Vortex Flow Devices," *J. Appl. Phys.*, vol. 76 (11), December, 1994.

[7] R. E. Eck, D. J. Scalapino, and B. N. Taylor, "Self-Detection of the ac Josephson Current," *Phys. Rev. Lett.*, vol. 13 (1), pp. 15–18, July, 1964.

[8] H. S. J. van der Zant, R. A. M. Receveur, and T. P. Orlando, "One-Dimensional Parallel Josephson Junction Arrays as a Tool for Diagnostics," *Appl. Phys. Lett.*, October, 1994.

[9] J. B. Hansen, "Noise in Superconducting Josephson Junctions," in *Non-Linear Superconductive Electronics and Josephson Devices*, G. Costible, S. Pagano, N. F. Pedersen, and M. Russo, Eds. New York: Plenum Press, 1991, pp. 161–180.

[10] S. Sakai, A. V. Ustinov, H. Kohlstedt, A. Petraglia, and N. F. Pedersen, "Theory and Experiment on Electromagnetic Wave Propogation Velocities in Stacked Superconducting Tunnel Structures," to be published.

[11] A. V. Ustinov, H. Kohlstedt, and C. Heiden, "Magnetic Flux Dynamics in Stacked Josephson Junctions," to be published.

[12] N. Grønbech-Jensen, M. R. Samuelsen, P. S. Lomdahl, and J. A. Blackburn, "Bunched Soliton States in Weakly Coupled Sine-Gordon Systems," *Phys. Rev. B*, vol. 42 (7), pp. 3976–3980, September, 1990.

Bibliography

[1] D. P. McGinnis, J. B. Beyer, and J. E. Nordman, "A Modified Superconducting Current Injection Transistor and Distributed Amplifier Design," *IEEE Trans. Mag.*, vol. 25, pp. 1262–1265, March 1989.

[2] B. J. Van Zeghbroeck, "Superconducting Current Injection Transistor", *Appl. Phys. Lett.*, vol. 42 (8), pp. 736–738, April 1983.

[3] D. Berman, H. S. J. van der Zant, and T. P. Orlando, "Discrete Superconducting Vortex Flow Transistors," *IEEE Trans. Appl. Superconductivity*, vol. 4, pp. 161–168, September 1994.

[4] D. P. McGinnis, J. E. Nordman, and J. B. Beyer, "Optimization of Circuit Parameters for the Vortex Flow Transistor," *IEEE Trans. Mag.*, vol. 23, pp. 699–702, March, 1987.

[5] Y. M. Zhang, D. Winkler, and T. Claeson, "Detection of MM and SUBMM Wave Radiation from Soliton and Flux-Flow Modes in a Long Josephson Junction," *IEEE Trans. Appl. Superconductivity*, vol. 3 (1), pp. 2520–2523, March, 1993.

[6] H. S. J. van der Zant and T. P. Orlando, "The Eck Peak in Underdamped Discrete Superconducting Vortex Flow Devices," *J. Appl. Phys.*, vol. 76 (11), December, 1994.

[7] R. E. Eck, D. J. Scalapino, and B. N. Taylor, "Self-Detection of the ac Josephson Current," *Phys. Rev. Lett.*, vol. 13 (1), pp. 15–18, July, 1964.

[8] H. S. J. van der Zant, R. A. M. Receveur, and T. P. Orlando, "One-Dimensional Parallel Josephson Junction Arrays as a Tool for Diagnostics," *Appl. Phys. Lett.*, October, 1994.

[9] J. B. Hansen, "Noise in Superconducting Josephson Junctions," in *Non-Linear Superconductive Electronics and Josephson Devices*, G. Costible, S. Pagano, N. F. Pedersen, and M. Russo, Eds. New York: Plenum Press, 1991, pp. 161–180.

[10] S. Sakai, A. V. Ustinov, H. Kohlstedt, A. Petraglia, and N. F. Pedersen, "Theory and Experiment on Electromagnetic Wave Propogation Velocities in Stacked Superconducting Tunnel Structures," *Phys. Rev. B*, vol. 50 (17), pp. 12905–12915, November, 1994.

[11] A. V. Ustinov, H. Kohlstedt, and C. Heiden, "Magnetic Flux Dynamics in Stacked Josephson Junctions," to be published.

[12] N. Grønbech-Jensen, M. R. Samuelsen, P. S. Lomdahl, and J. A. Blackburn, "Bunched Soliton States in Weakly Coupled Sine-Gordon Systems," *Phys. Rev. B*, vol. 42 (7), pp. 3976–3980, September, 1990.

[13] H. Kohlstedt, A. V. Ustinov, M. Cirillo, and G. Hallamanns, "Investigation of Coupling Between Long Vertically Stacked Nb-Al/AlO_x-Nb Josephson Tunnel Junctions," Velocities in Stacked Superconducting Tunnel Structures," *EUCAS/*, vol. 50 (17), October, 1993.

[14] A. V. Ustinov, H. Kohlstedt, and C. Heiden, "Coherent Flux Flow in Vertically Stacked Long Josephson Tunnel Junctions," *ASC/*, October, 1994.

[15] T. P. Orlando, K. A. Delin, *Foundations of Applied Superconductivity.* New York: Addison-Wesley, 1991, pp. 160–171,291–292,398–407.

[16] B. D. Josephson, "Weakly Coupled Superconductors", in *Superconductivity*, vol. 1, R. D. Parks, Ed. New York: Marcel Dekker, 1969.

[17] W. C. Stewart, "Current-Voltage Characteristics of Josephson Junctions," *Appl. Phys. Lett.*, vol. 12, pp. 277–280, April, 1968.

[18] D. E. McCumber, "Effect of an ac impedance on dc voltage-current characteristics of superconductor weak-link junctions," *J. Appl. Phys.*, vol. 39, pp. 3113–3118, June, 1968.

[19] K. K. Likharev, *Dynamics of Josephson Junctions and Circuits.* Gordon and Breach, 1986.

[20] B. D. Josephson, "Supercurrents through Barriers", *Advan. Phys.*, vol. 14, pp. 419–451, October, 1965.

[21] E. Trias, "Inductance Effects in Two-Dimensional Arrays of Josephson Junctions," Master's thesis, MIT. May, 1995, unpublished.

[22] S. Watanabe, H. S. J. van der Zant, S. H. Strogatz, and T. P. Orlando, "Dynamics of circular Josephson junction arrays and the discrete sine-Gordon equation," unpublished.

[23] D. D. Coon and M. D. Fiske, "Josephson ac and Step Structure in the Supercurrent Tunneling Characteristic," *Phys. Rev.*, vol. 138 (3A), pp. 744–746, May 1965.

[24] T. A. Fulton and R. C. Dynes, "Single vortex propogation in Josephson tunnel junctions," *Solid State Comm.*, vol. 12, pp. 57–61, 1973.

[25] R. E. Eck, D. J. Scalapino, and B. N. Taylor, "Self-Detection of the ac Josephson Current," *Phys. Rev. Lett.*, vol. 13 (1), pp. 15–18, July 1964.

[26] H. S. J. van der Zant, D. Berman, and T. P. Orlando, "Fiske modes in one-dimensional parallel Josephson-junction arrays," *Phys. Rev. B*, vol. 49 (18), pp. 12945–12951, May 1994.

[27] Hypres, Inc. Elmsford, NY

[28] V. Ambegaokar and A. Baratoff, "Tunneling between superconductors," *Phys. Rev. Lett.*, vol. 10, pp. 486–489, 1963.

[29] C. S. Owen and D. J. Scalapino, "Vortex Structure and Critical Currents in Josephson Junctions," *Phys. Rev.*, vol. 164 (2), pp. 538–544, 1967.

[30] A. Barone and G. Paterno, *Physics and Applications of the Josephson Effect*, John Wiley and Sons, 1982, pp. 100–112.

[31] H. A. Haus and J. R. Melcher, *Electromagnetic Fields and Energy.* Prentice-Hall, 1989, pp. 471–472.

[32] S. Watanabe, *Nonlinear Dynamics of One-Dimensional Josephson Junction Arrays.* Ph. D. thesis, MIT. May, 1995. unpublished.